TEMPLATED SYNTHESIS AND CHARACTERIZATIONS OF HIGH MOMENT MAGNETIC NANOPARTICLES FOR BIOAPPLICATIONS

by

PUNNAPOB PUNNAKITIKASHEM

Presented to the Faculty of the Graduate School of

The University of Texas at Arlington in Partial Fulfillment

of the Requirements

for the Degree of

DOCTOR OF PHILOSOPHY

THE UNIVERSITY OF TEXAS AT ARLINGTON

May 2011

The dissertation is dedicated to my father and mother

ACKNOWLEDGEMENTS

My deep gratitude goes to my advisor, Dr. Yaowu Hao, for his advice during my doctoral studies. He introduced me to a very interesting research topic and also consistently helped me in my research. I appreciate his thinking, taking time answering, and guiding through many challenges. I am highly grateful to my supervising committee, Dr. Ali R. Koymen, Dr. Pranesh Aswath, Dr. Choong-Un Kim, Dr. Fuqiang Liu, and Dr. J. Ping Liu, for their encouragement and helpful advice in my research.

I want to thank all my labmates, Shih-Hsin Chang, Chien-Wen Huang, Chivarat Muangphat, Orathai Thumthan, Jiaqi Wu, Megha Panuganti, Rishi Wadhwa, Jingwen He, and Yi-Jiun Li, for their friendships and useful discussions. I would also like to thank the other labs that helped in completing in my research work, Nanotechnology Research and Training Facility, Nanostructured Magnetic Materials Lab, and Characterization Center for Materials & Biology, for their excellent training on equipments.

I highly appreciate to all my family members for their inspiration, unconditional love, persistent support. I am indebted to the loving memory of my aunt, Atchawee Luisiri, for her love and support. I also want to express my sincere appreciation to my grandparents, aunts, uncles for their encouragement.

April 25, 2011

ABSTRACT

TEMPLATED SYNTHESIS AND CHARACTERIZATIONS OF HIGH MOMENT MAGNETIC NANOPARTICLES FOR BIOAPPLICATIONS

Punnapob Punnakitikashem, Ph.D.

The University of Texas at Arlington, 2011

Supervising Professor: Yaowu Hao

Magnetic nanoparticles have been widely used for biomedical applications such as drug and gene delivery, hyperthermia treatment of cancer, MRI contrast enhancement, cell labeling and magnetic separation. We present two new types of magnetic nanoparticles for bioapplications; granular superparamagnetic gold nanoparticles and multilayered nanodisks. Granular superparamagnetic gold nanoparticles consist of superparamagnetic islands embedded in a gold matrix. Multilayered nanodisks consist of two magnetic layers separated by a non-magnetic layer with two capping layers. Capping layers such as gold provide functionalization sites for biomolecule attachment. These nanoparticles possess two key magnetic requirements for bioapplications, a high saturation magnetic moment and a near-zero remanence, and have a great potential of combining both magnetic and gold nanoparticle into one nanoentity to provide multifunctionality.

A scalable, inexpensive, and simple template-based synthesis process to produce nanoparticles in large quantity has been developed. Anodic aluminum oxide (AAO) has been utilized to generate very large area templates with feature size ranging from 20 nm to 100 nm. Thick and ultra thin (< 200 nm) AAO templates have been successfully fabricated by anodization. The anodization process of ultra thin AAO has been studied. Using such template, a new type of nanoparticle, truncated hollow cones, can be produced. Multilayered and granular nanodisks have been fabricated by evaporation and electrodeposition into the AAO templates and their magnetic properties have been characterized. Using thick AAO template, multilayered or granular nanodisks are deposited through electrodeposition. A one-bath electrolyte has been developed to deposit both gold and magnetic materials (Co and Fe). The designed properties have been achieved for such nanodisks, including high moment, low remanence and tunable saturation field. Pillar-template has been generated using the thick AAO template, and has also been explored to fabricate nanodisks in large quantity.

TABLE OF CONTENTS

LIST OF ILLUSTRATIONS

LIST OF TABLES

CHAPTER 1

INTRODUCTION

1.1. Introduction

Magnetic nanoparticles are being extensively used for biomedical applications such as cell separation, targeted drug and gene delivery, hyperthermia treatment, biophysics, and biosensors [1-3]. Magnetic nanoparticles can be controlled by external magnetic field gradient; therefore these particles can be used for bioseparation and can act as drug carrier to deliver to specific targets. When an AC magnetic field of sufficient strength and frequency is applied to magnetic particles attached to diseased tissue, heat is generated that can be used for the treatment of the diseases [4]. Magnetic nanoparticles have emerged as a new platform technology for biosensor development. This technology is based on the detection of biologically functionalized magnetic particles, using high-sensitivity microfabricated magnetic-field sensors [5]. Recently, these increasing research activities form the new research field of biomagnetics [6].

Superparamagnetic nanoparticles play an important role in the development of biomagnetics [7]. Superparamagnetic is a special state of ferromagnetic. Similar to ferromagnetic materials, superparamagnetic can be saturated at a low external magnetic field, obtaining much higher saturation magnetic moment than paramagnetic materials, typically 10^4 times higher. However, unlike normal ferromagnetic materials, these nanoparticles have no remanent moment, similar to

paramagnetic materials. This unique property nonmagnetism without external magnetic field avoids nanoparticles from the aggregation due to the magnetic attraction which is desirable for biomedical applications. Recently, superparamagnetic nanoparticles are commercially available for magnetic resonance imaging (MRI) contrast agent and magnetic cell separation. For MRI, small iron oxide particles (<20 nm) coated with a biocompatible polymer are usually used. For cell separation, large (>1 μm) spherical beads consisting of dispersed iron oxide particles in polymer matrix are commonly used. Embedding multiple nanoparticles in a polymer matrix can generate large magnetic moment while still keeping superparamagnetic characteristics, but the size of entire particle become very large due to the low percentage of embedded magnetic materials, typically 10-20%, to avoid interaction between magnetic nanoparticles. Superparamagnetic nanoparticles embedded in polymer matrix have very large size in micron scale in order to have enough magnetic moment. If the size of entire particles is too small, the magnetic moment of the particles becomes very low.

In this research, two new types of magnetic nanoparticles, multilayered and graunular magnetic nanodisks, as shown in Figure 1.1, are designed and fabricated. In these nanoparticles, two important requirements for bioapplications, high magnetic moment and near-zero remanence, are achieved. Multilayered nanodisks consist of two magnetic layers separated by a non-magnetic layer with two capping layers. Magnetic properties are controlled by magnetostatic interlayer coupling between two magnetic layer. Capping layers such as gold provide functionalization sites for biomolecule attachment. For granular magnetic nanodisk, superparamagnetic nanoparticles are embedded in gold matrix; resulting in a combination of the

properties from both gold and magnetic nanoparticles. Such nanoparticle can be dragged by magnetic field gradient as well as exhibits surface plasmon resonance from gold. The size of these nanoparticles ranges from 20-100nm, while commercial magnetic particles with superparamagnetic nanoparticles embeded in a polymer matrix need micronmeter size to have the equivalent magnetic moment. Therefore, these nanodisks provide many new possibilities for biomagnetic applications.

Figure 1.1 Configurations of multilayered (left) and granular (right) magnetic nanodisk.

In this research, an inexpensive and simple template-directed synthesis method to fabricate nanodisks has been developed. To fabricate designed nanodisks, we have developed template growth methods. The general process is illustrated in Figure 1.2. Either pillar-template or hole-template can be used. First, a sacrificial layer, which can be SiO_2, Cu, Al, or even NaCl, is deposited at the bottom. Different materials are either electrodeposited or vacuum evaporated into template holes or on the top of the template pillars. After the deposition, the sacrificial layer can be selectively dissolved to release nanodisks into solution. Electrodeposition can only use hole-templates and evaporation process can use either hole templates or pillar templates. Hole templates need to be destroyed to release nanodisks into solution. Pillar templates can be reusable after cleaning the deposited material.

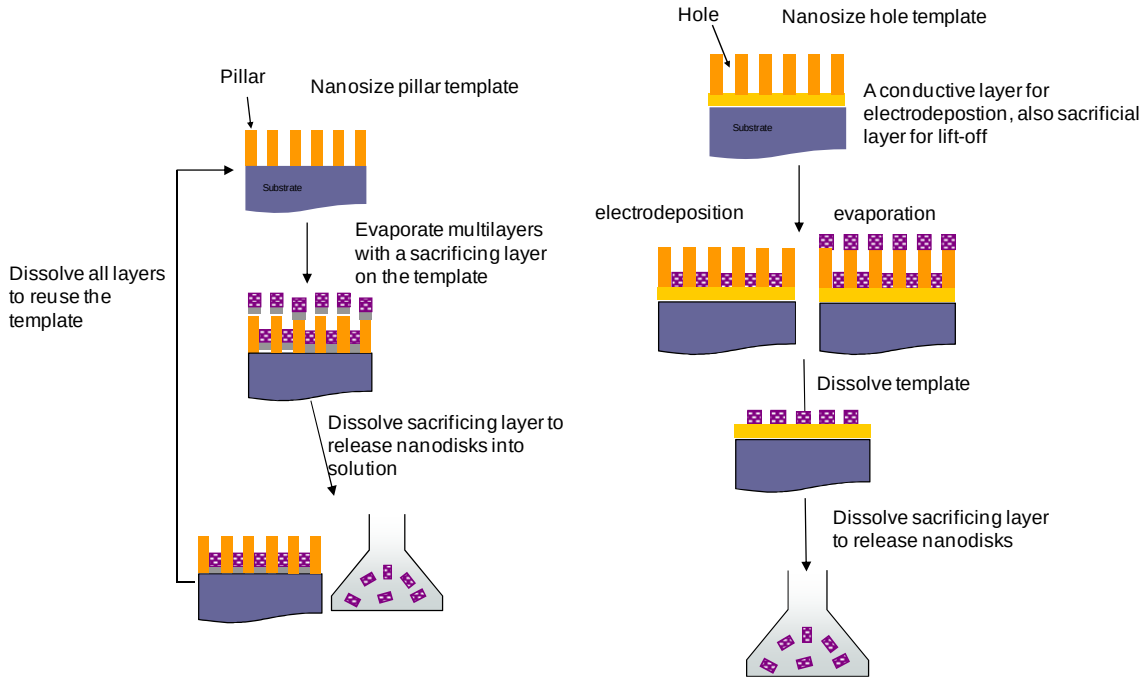

Figure 1.2 General processes of fabricating magnetic nanodisks.

The proposed process is crucially dependent on high through-put very large area sub-100 nm simple nanopattern generation tools. Conventional photolithography and electron-beam lithography are not economically feasible for this purpose.

Porous anodic aluminum oxide (AAO) has been selected as the template because it provides several unique features such as large area, small size, short operation time, and no vacuum needed. Thick and ultra thin AAO templates have been successfully fabricated by anodization. The anodization process of ultra thin AAO has been studied. Using such template, a new type of nanoparticle, truncated hollow cones, can be produced. Multilayered and granular nanodisks have been fabricated by evaporation and electrodeposition into the AAO templates and their magnetic properties have been characterized. Using thick AAO template,

multilayered or granular nanodisks are deposited through electrodeposition. A one-bath electrolyte has been developed to deposit both gold and magnetic materials (Co and Fe). The deposition time of both gold and magnetic are varied to manipulate the thickness to achieve the desired magnetic property. Ultra thin (below 200 nm) AAO template is used to produce nanodisks using evaporation. The designed properties have been achieved, including high moment, low remanence and tunable saturation field. Pillar-template has been generated using thick AAO template, and is employed to fabricate nanodisks in large quantity with a diameter of 70 nm and a thickness of 60 nm. The magnetic characterization shows that each nanodisk possesses a magnetic moment equivalent to 100 10-nm Co nanoparticles and a near-zero remanent moment.

1.2. Dissertation objectives and outline

The objective of this research is to develop new types of magnetic nanoparticles with a size ranging from 20 to 100 nm which can potentially replace iron oxide superparamagnetic nanoparticles bioapplications, offering high magnetic moment for individual particles. Moreover, the saturation field of these nanoparticles can be tuned, which could open other possibilities for bioapplications. We propose to use template-directed synthesis method to fabricate these particles. The template must be inexpensive for this purpose. Because of this requirement, anodic alumina has been chosen.

The outline of this dissertation is as follows. In Chapter 2, brief background information on the magnetic nanoparticle and the anodic alumina is given. In Chapter 3, the designs of magnetic nanoparticle are presented. The experimental methods

are explained in chapter 4. In Chapter 5, the anodization of ultra thin aluminum on silicon substrates are discussed. In chapter 6, the fabrication of designed magnetic nanodisks using ultra thin alumina is discussed. In Chapter 7, the fabrication of magnetic-gold nanoparticle using one-bath electrodeposition process is described. In chapter 8, the fabrication of multilayered magnetic nanodisks by the pillar-template method is described. In Chapter 9, the contributions of this research are summarized.

CHAPTER 2

BACKGROUND INFORMATION

In this chapter, magnetic properties of magnetic nanoparticles are first introduced starting with the energy terms associated with magnetic materials with very small sizes. Then, synthesis, properties and applications of superparamagnetic nanoparticles are described. A brief description of the principle of anodization of aluminum is also included in this chapter.

2.1. Magnetic nanoparticles

2.1.1. Energy terms associated with small magnetic structures

A full understanding of the magnetic properties of magnetic nanoparticles can be achieved by considering all associated energy terms.

Thermal energy

Thermal energy acts to randomize the materials, so that the random direction of magnetization increases at elevated temperature. This energy can act either on atomic magnetic materials or entire particles. The value of thermal energy is a function of kT .

Exchange energy

Exchange energy measures the interaction of spin between two electrons. Exchange energy in ferromagnetic materials has a tendency to keep adjacent

magnetic moments aligned in the same direction to each other. Therefore, uniform magnetization has minimum exchange energy.

Zeeman energy

Zeeman energy can be referred to as magnetic potential energy. This energy is the tendency of the magnetization to align in an external magnetic field and is always minimized when the magnetization direction is aligned in the same direction as the externally applied magnetic field. The equation is given by

$$E_z = -\overrightarrow{H}_{ext} \bullet \overrightarrow{M}$$

where $\overrightarrow{H}_{ext}$ is the external field vector, and $\overrightarrow{M}$ is the magnetization vector.

Magnetostatic energy

In any magnetized magnetic specimen, there is a demagnetizing field inside the magnet which is in the opposite direction of the magnetization direction. This self-demagnetizing action tends to break magnet into two domains in order to reduce the total magnetostatic energy. Even though the formation of two domains increases the exchange energy, anisotropy energy, but total energy is decreased by reduction of magnetostatic energy. The magnetostatic energy is dependent on shape of the specimen. The magnetostatic energy is expressed as

$$E_{ms} = \frac{1}{2} H_d M$$

where H_d is a demagnetizing field of magnetic materials, and M is magnetization.

Anisotropy energy

Magnetic materials have a preferential direction for the magnetization to point to, which is called anisotropy. Two types of anisotropy need to be considered in

nanomagnets; magnetocrystalline anisotropy or crystalline anisotropy, and shape anisotropy. First, crystalline anisotropy is a tendency of magnetization to align in a particular crystalline direction. The uniaxial anisotropy energy is given by

$$E_{ani} = K_{u1} \sin^2 \theta + K_{u2} \sin^4 \theta$$

where K_{u1} and K_{u2} are anisotropy energy constants, and θ is angle between magnetization direction and easy axis orientation. In a cubic system, an anisotropy energy density can be written as

$$E_{ani} = K_1(\alpha_1^2\alpha_2^2 + \alpha_2^2\alpha_3^2 + \alpha_3^2\alpha_1^2) + K_2(\alpha_1^2\alpha_2^2\alpha_3^2)$$

where K_1 and K_2 are anisotropy constants, and α_1, α_2, and α_3 are the projections of the unit vector on three crystalline easy axes. HCP cobalt has a uniaxial crystalline anisotropy with easy axis in basal plan [0001] direction, while FCC Ni and BCC Fe have a cubic crystalline anisotropy with easy axis in [111] direction for Ni and [100] direction for Fe.

Second, if the specimen is in spherical shape and has no magnetocrystalline anisotropy, the applied field will magnetize the specimen to have the same magnetization in any direction. For a non-spherical specimen with no magnetocrystalline anisotropy, magnetization direction points to the elongated axis of the specimen. This phenomenon is called shape anisotropy.

2.1.2. Size effect of magnetic properties of nanoparticles

Size of a ferromagnetic material has important effects on its magnetic properties. Magnetic materials can be divided into three size categories; multidomain, single domain and superparamagnetic. For nanoparticles, the size

boundary between these categories are considered below; the single-domain limit and the superparamagnetic limit.

Single domain particle

In magnetic bulk materials, there exists a multidomain structure contributed by regions of the magnetic moments that aligned in parallel and separated from the each other by domain walls. Each domain has its own magnetization from an alignment of atomic magnetic moment within the domain. The size and shape of these domains depend on the interaction between the exchange, magnetostatic, and anisotropy energies of the system. There is a balance between the magnetostatic energy (ΔE_{MS}) and the domain-wall energy (E_{dw}) in the formation of the domains wall process. As the volume of the magnetic nanoparticles decreases, the size of the domain and width are reduced. At a certain volume, the energy to produce domain wall is larger than the corresponding reduction of the magnetostatic energy. The particle no longer divides into smaller domains, but maintains single domain. This critical size ranges in a few tens of nanometers and depends on the saturation magnetization of the particle, anisotropy energy and exchange interactions. The critical diameter of a spherical particle, D_c, when it reaches a single domain state can be calculated when $\Delta E_{MS} = E_{dw}$. The equation to find critical value is given by

$$D_c = 18\sqrt{AK_a} / \left(\mu_o M^2\right)$$

where A is the exchange constant, K_{eff} is anisotropy constant, μ_0 is the vacuum permeability, and M is the saturation magnetization. For example, the critical values for Fe and Ni particles are 15 and 55 nm, respectively, while $SmCo_5$ particle is 750 nm, as shown in Table 2.1 [8].

Table 2.1 Estimated single domain size for different special particles [8].

Material	Dc (nm)
Co (HCP)	15
Co (FCC)	7
Fe	15
Ni	55
$SmCo_5$	750
Fe_3O_4	128

If a magnetic sample is placed in an applied external magnetic field (H), a typical hysteresis loop as shown in Figure 2.1 is obtained showing that the magnetization (M) increases with H until a saturation M_s value is reached. When H returns to zero, there is remanence M_R indicating that magnetic sample is a strong magnet. To remove M_R, a coercive field H_C has to be applied in the opposite direction of the initially applied field. Very high remanence is observed in a small single-domain nanoparticle, since a single-domain particle is uniformly magnetized with all the spins aligned in the same direction. But, as the size of a single domain magnetic becomes smaller, the remanence and coercivity will decrease, and at certain size, it can go to zero, which is termed as superparamagnetic state.

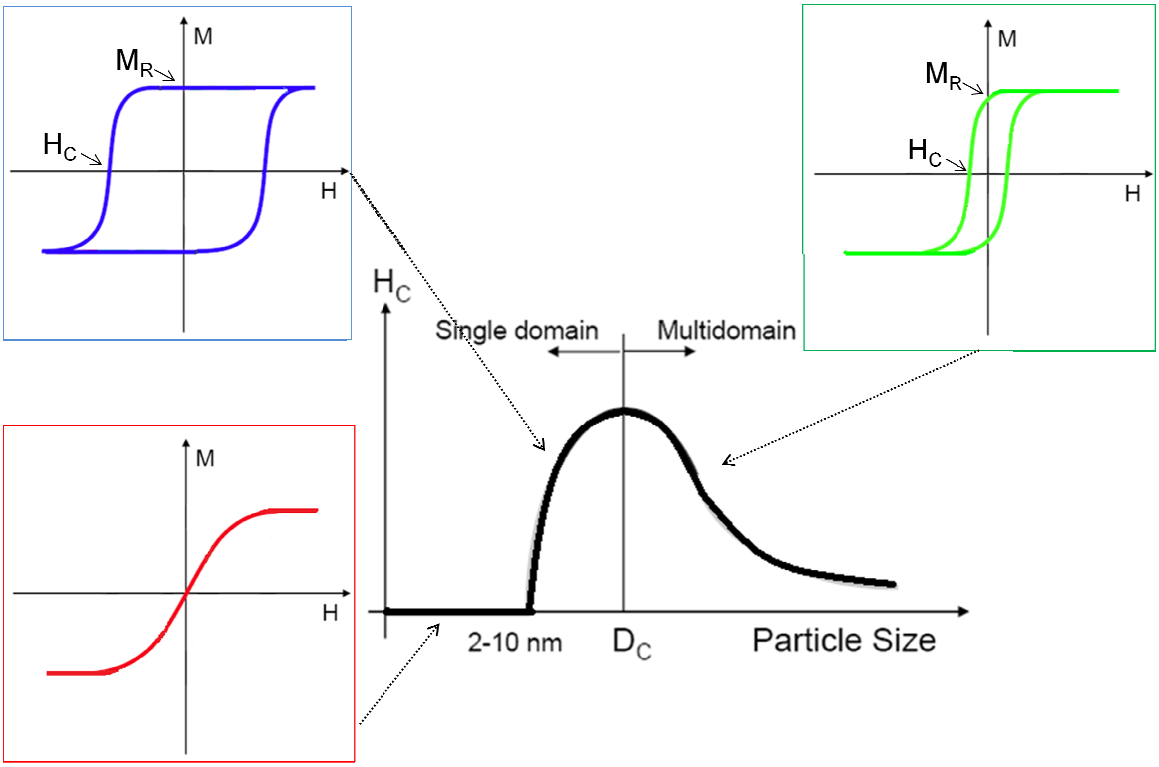

Figure 2.1 Typical hysteresis loops of multidomain, single domain, and superparamagnetic particles.

Superparamagnetism

Superparamagnetic nanoparticles can occur only in very small ferromagnetic nanoparticles at room temperature. For example, the critical sizes of superparamagnetic Co and Fe are estimated as 7 nm and 6 nm, respectively. The superparamagnetic phenomenon can be explained as that the thermal energy, kT , is sufficient to cause fluctuation of magnetization, leading to zero remanence and zero coercivity. Superparamagentic behavior is desirable for biomedical applications. Superparamagnetic iron oxide nanoparticles have been one of the commonly used materials in biomedical applications.

The switching of magnetization from one direction to the opposite direction (fluctuation of magnetization) can be considered as a thermally activated process (jumping over an energy barrier). The thermal energy in superparamagnetic

nanoparticle is large enough to overcome anisotropy energy barrier, KV, to cause fluctuation of magnetization direction, as shown in Figure 2.2. This energy barrier is related to intrinsic and extrinsic effects such as magneto-crystalline and shape anisotropies.

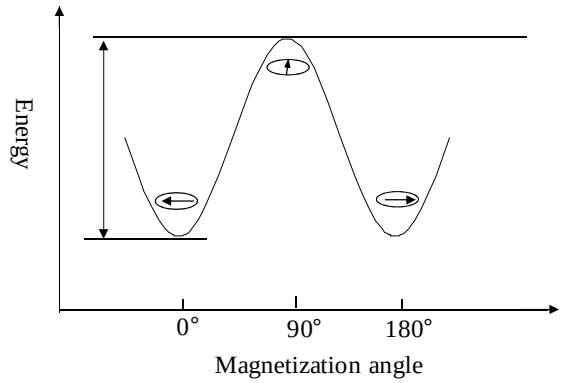

Figure 2.2 The process of magnetization switching can be viewed as overcoming anisotropy energy barrier at finite temperature.

In superparamagnetic state, the remanence no longer exists because the moment jumps between two different preferred orientations of magnetization. In this thermally activated process, there is a finite probability of the magnetization switching. The switching probability per unit time *r* can be described by the Arrhenius relation. The Arrhenius equation is given by:

$$r = f_o e^{-\frac{\Delta E}{kT}}$$

where f_o is the thermal attempting frequency, which is related to materials properties, and the typical value is 10^9 s^{-1}, ΔE is the single energy barrier; *k* is Boltzmann constant; and *T* is temperature.

Superparamagnetic nanoparticles are dependent not only on temperature, but also on the measurement time. Relaxation time (τ) is the reciprocal of switching probability (*r*). If measurement time is much shorter than the relaxation time of nanoparticles which means that the switching is slower compared to measurement

time, the magnetization of a particle will be still observed. However, when measurement time is much longer than the relaxation time, the average net magnetization of a particle will be zero, which is considered as superparamagnetic.

2.1.3. Synthesis of magnetic nanoparticles

Magnetic nanoparticles have been synthesized using several techniques such as, co-precipitation, thermal decomposition, and micelle synthesis. Superparamagnetic iron oxide nanoparticles, Fe_3O_4 or magnetite, are usually synthesized by wet chemical procedure, commonly by co-precipitation-based method. Co-precipitation has several advantages such as short synthesis time, simple technique, narrow size distribution, high yield, easy to control [9]. The size, shape, and composition of magnetite can be controlled by the type of salt solution that is nitrides, chlorides, or sulfates. For example, ferrous chloride ($FeCl_2$) and ferric chloride ($FeCl_3$) are commonly used as reactants and are mixed in water to become aqueous Fe^{2+} and Fe^{3+} salt solutions. A base solution is added in such salt solutions to form magnetite at room temperature or at elevated temperature through the reaction

$$Fe^{2+} + 2Fe^{3+} + 8OH^- \rightarrow Fe_3O_4 + 4H_2O$$

In general, magnetite nanoparticles are very easily oxidized to form maghemite (γ-Fe_2O_3) due to their instability which decrease the magnetic moment. Moreover, the particles produced by co-precipitation tend to aggregate together. To produce monodisperse particles, a short-burst nucleation and slow growth control is very crucial. Organic additives such as polyvinylalcohel (PVA) are used as stabilizing agents [10]. Normally, size of these particles ranges from 4 to 20 nm and the

magnetic moment of these iron oxide superparamagnetic nanoparticles ranges from 30-50 emu/g, which is much lower than the bulk value, 92 emu/g [9, 11].

2.2. Nanosized template generation

There are many nano-patterning methods to produce nanosized templates (holes or pillars), including lithographic methods (such as electron-beam, ion-beam, and x-ray lithography), self-assembly of nanoparticles, and scanning probe techniques [12-16]. These techniques can be used to successfully produce metal or semiconductor nanostructures on substrates. Electron beam lithography is the most general lithography tool because it provides precise control over size, shape, and spacing of the nanostructures. Using self-assembly of nanoparticles can large area of periodic structures can be obtained. Scanning probe technique is to use either scanning tunneling microscopy or atomic force microscopy to create nanopatterns. However, these methods are not suitable to generate templates for our purpose. The electron beam lithography is a time-consuming process with low throughput, and high costs. The self-assembly processes have a poor control over the size distribution and are difficult to keep substrate clean because of byproducts generated from wet-chemical preparation. The scanning probe technique cannot be produced in large areas because the writing process is very slow.

Anodization of aluminum is a simple nano-pattern generation method. It can produce large area of nanoscale features. This process has been chosen to generate templates for the fabrication of designed nanodiskd. To fabricate nanomaterials, anodic porous alumina (Al_2O_3) is used as a templating process with

features such as small size, large amount of particles, simple generation tool, no vacuum needed, short operation time, and high structural controllability is desired.

Anodization of aluminum

In an acidic electrolyte and under high voltage, anodization of bulk aluminum (Al) can produce porous structures having highly ordered pore arrays in the nanometer range, as shown in Figure 2.3a-c [17]. The geometry of anodic porous alumina is represented as a close-packed array of columnar hexagonal cells, each containing a cylindrical center pore that is perpendicular to the substrate, as shown in Figure 2.3d. The cylindrical pores have a downward direction to an alumina oxide barrier layer located between pore bottom and the substrate. The alumina oxide barrier layer has U-shape geometry, and its thickness is only half of the pore wall. The pore diameter is between one third and half of the cell size. Using selected acid solutions, such as phosphoric acid to etch and widen oxide aluminum, pore diameters can be tuned within the cell size.

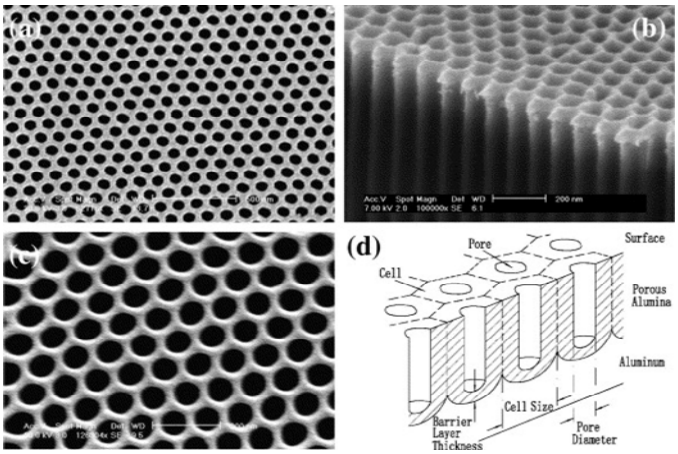

Figure 2.3 SEM micrographs of porous alumina a) top b) cross-section c) after pore widening, d) configuration diagram [18].

The advantage of the anodic porous alumina is that the pore diameter and cell size can be tuned [19-22]. The pore diameter of porous alumina is proportional to the applied anodizing voltage. There are many kinds of electrolytes for anodization that can be used, including sulfuric, phosphoric, and oxalic acid which affect cell size, pore diameter, and spacing [23]. The sulfuric acid is suitable for porous alumina with pore diameter about 10-30 nm; the oxalic acid is suitable to fabricate porous alumina with medium-sized pores ranging from 30 nm to 80 nm, and the phosphoric acid is proper to produce anodic alumina with pore diameter larger than 80 nm. The narrow distribution of pore diameter and cell size, and regular arrangement can be obtained for small and medium-sized pores. On the other hand, it is difficult to achieve a regular arrangement and uniform pore diameter using phosphoric acid.

A possible mechanism for pore formation in porous alumina is provided based on the chemical processes listed below [24].

First, Al^{3+} ions form at the metal/oxide interface and migrate into the oxide layer near the oxide/metal interface.

$$Al(s) \rightarrow Al^{3+}\ (oxide) + 3e^{-}$$

Second, at the oxide/electrolyte interface, the water splitting reaction occurs at the pore bottom.

$$2H_2O \rightarrow 2O^{2-}\ (oxide) + 4H^{+}\ (aq)$$

Third, due to the electric field, the O^{2-} ions migrate within the oxide layer from the oxide/electrolyte interface toward the metal/oxide interface. And Al^{3+} move toward the oxide/electrolyte interface. Usually, cations have higher diffusivities than anion in oxide layer. The O^{2-} (oxide) ions reacts with the Al^{3+} (oxide) ions to form Al_2O_3.

$$2Al^{3+} + 3O^{2-} \rightarrow Al_2O_3\ (s)$$

Fourth, there is electric-field-enhanced oxide dissolution; protons can locally dissolve oxide at the oxide/electrolyte interface. It is because of this step, pores can form.

$$Al_2O_3\ (s) + 6H^{+}\ (aq) \rightarrow 2Al^{3+}\ (aq) + 3H_2O\ (aq)$$

Finally, hydronium ions can migrate toward the cathode, where they react with electrons to form H_2 gas, completing the circuit.

$$6H^{+}\ (aq) + 6e^{-} \rightarrow H_2\ (g)$$

There is a balance between the electric-field-enhanced oxide dissolution at electrolyte/oxide interface and formation of oxide at metal/oxide interface in the anodization process. This is very important for the formation of the porous alumina because thickness of the barrier layer is constant in the entire process that allows steady-state pore propagation. The absence of electric-field-enhanced oxide dissolution will just make barrier-type non-porous alumina anodized in neutral or base solutions.

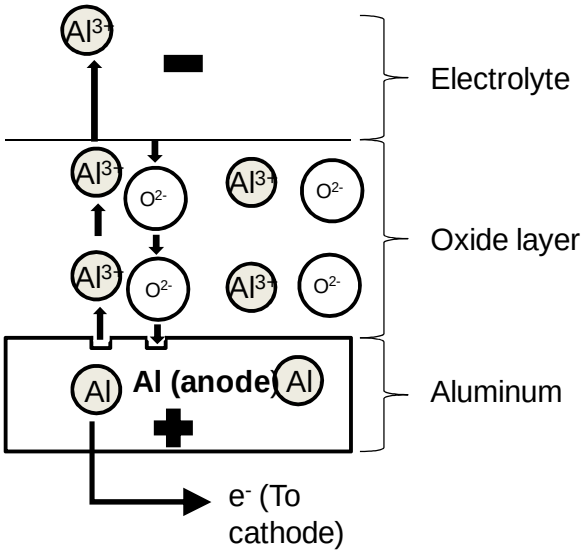

Figure 2.4 Schematic drawing of the electric-field-enhanced diffusion of aluminum and oxygen ions.

CHAPTER 3

DESIGN OF HIGH MOMENT MAGNETIC NANOPARTICLES FOR BIOAPPLICATIONS

Explorations of magnetic nanoparticles for bioapplications such as targeted drug and gene delivery, hyperthermia treatment, cell and DNA mechanics, and biosensors have attracted much more attentions [25-35]. These rapidly increasing research activities form the research field of “biomagnetics”. Superparamagnetism theory and handily available superparamagnetic nanoparticles played crucial roles in the development of biomagnetics [36, 37]. Superparamagnetic particles can be saturated at a low external magnetic field. At the same time, they have no remanent moment, i.e. they appear nonmagnetic without external magnetic field. This unique property keeps nanoparticles from the aggregation due to the magnetic attraction. Now, superparamagnetic iron oxide nanoparticles are commercially available for magnetic resonance imaging (MRI) contrast agents and magnetic cell separation. For MRI, small iron oxide particles (<20 nm) coated with a biocompatible polymer are usually used [38]. For cell separation, large (>1 μm) spherical beads consisting of dispersed iron oxide particles in a polymer matrix are commonly used to get enough magnetic force [39]. Most research on other new biomagnetic applications has conveniently utilized these magnetic nanoparticles, and has produced many promising results.

However, the superparamagnetic phenomenon only occurs in very small nanoparticles at room temperature. For example, the critical sizes at which superparamagnetic occurs at room temperature are estimated as 7 nm for Co and 6 nm for Fe. Small size results in a small net magnetic moment. For some biomagnetic applications such as magnetic biosensing, cell mechanics, and drug and gene targeted delivery; there exists a minimum net magnetic moment requirement for individual particles to generate enough magnetic signals or magnetic forces. To obtain a high magnetic moment, simply making particles larger cannot be an option at all, resulting in a strong aggregation due to the magnetic attraction since particles are no longer superparamagnetic. Embedding multiple nanoparticles in a matrix can generate large magnetic moment while still keeping superparamagnetic characteristics, but the size of the entire particle becomes very large due to the low percentage of embedded magnetic nanoparticles, typically 10-20%, to avoid interaction between magnetic nanoparticles. Moreover, the size of the particles is another very important parameter for bioapplications, usually the smaller the better. For example, magnetic nanoparticles for cell mechanics study, in which many nanoparticles can be manipulated simultaneously inside a cell (10 - 100 μm) by an external magnetic field, nanoparticles should possess high moments to generate enough force, and at the same time the sizes should be smaller than 100 nm so that they can easily diffuse in the actin network into different part of the cell. Another example is magnetic DNA microarray technology, where both magnetic moment and particle size are determining factors for its ultimate sensitivity [5]. It can be seen that for many biomagnetics applications available superparamagnetic particles are either

too small (<20nm) to posses enough magnetic moment or too big (>200nm) to have optimum performance.

Biomagnetics research field is growing rapidly; hundreds of scientific research papers are being published every year. However, all these new developments have focused on functionalization and applications of iron oxide nanoparticles, there is very few investigations on high moment magnetic nanoparticles. Very recently, synthetic antiferromagnetic (SAF) nanoparticles have been designed and fabricated [40, 41]. These nanoparticles consist of a stack of Ta/Ru/CoFe/Ru/CoFe/Ru/Ta, and antiferromagnetic coupling through Ru layer is utilized to make a zero remanence. Their fabrication process involved sputtering deposition of films, nanoimprint lithography (NIL) for pattern generation and ion milling for pattern transfer. The particles showed high moments and tunable saturation fields. But the complicated particle structure and fabrication process make these nanoparticles much more expensive, and therefore it may not be practical for typical bioapplications.

Here, we propose two new types of magnetic nanoparticles for biomedical applications, namely, multilayered magnetic nanodisks and granular superparamagnetic nanodisks.

3.1. Multilayered magnetic nanodisks

The configuration of a multilayered magnetic nanodisk is shown in Figure 3.1. It consists of two magnetic layers separated by a nonmagnetic spacing layer. The spacing layer acts as artificial domain wall to break magnetic single domain into two domains. Magnetizations in two single domain layers tend to point in the opposite

direction to minimize the magnetostatic energy. In other words, two magnetic layers have an interaction with each other, and the particles do not attract each other.

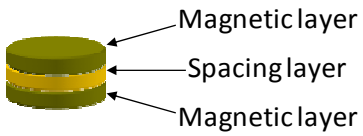

Figure 3.1 Configuration of the multilayered magnetic nanodisks.

3.1.1. General properties of multilayered magnetic nanodisks

The particle size in this design is usually single domain range, resulting in high remanence state. However, in this configuration, inserting an artificial domain wall causes the particle to have two domains, resulting in magnetostatic coupling between magnetic layers. The strong interaction of magnetostatic interlayer makes the particle to have low remanent moment. By adjusting the thicknesses of magnetic layers and spacing layer, a near to zero remanence in a range of external fields can be achieve, as shown in the hysteresis loop in Figure 3.2.

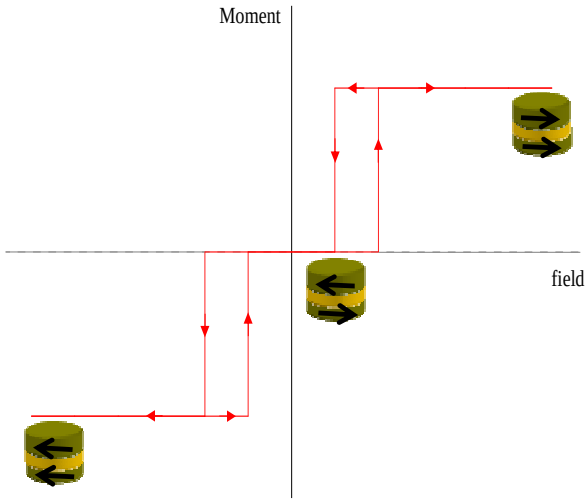

Figure 3.2 Expected hysteresis loop of the multilayered magnetic nanodisks.

Non-magnetic layers in the nanoparticles, including top, bottom and spacing layers, are anchorage sites for surface modification and functionalization, as shown in Figure 3.3. Commonly used inorganic materials for bioapplications, such as gold and silica, can be used. Surface modification and functionalization for gold and silica nanoparticles have been reported in many literatures. Another advantage of these multilayered nanodisks is that top and bottom surfaces can be made from different materials. For example, using Au and silica to cover two surfaces, thiolated DNAs can be selectively attached only to Au surface with silica surface passivated.

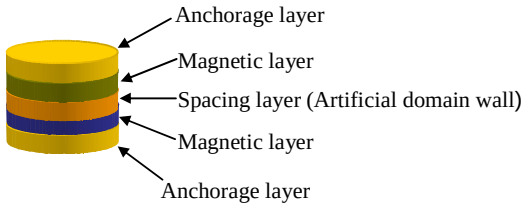

Figure 3.3 Configuration of the multilayered magnetic nanodisks with anchorage layers.

3.1.2. Tuning magnetic properties

Remanence moment, saturation magnetic moment, and saturation field are fundamental properties of these nanodisks for bioapplications. To avoid the strong magnetic attraction, zero or near zero remanence is required for bioapplications. Saturation magnetic moment determines the magnetic forces and magnetic signals for the nanodisks. High saturation magnetic moment benefits all bioapplications. Saturation field is the applied external field needed for nanodisks to reach their saturation moment. For biomagnetic applications, a low saturation field is usually desired. These three magnetic properties can be tuned by varying magnetic materials, sizes and thicknesses of magnetic layers.

Remanence moment

To get a near-zero remanence, the relative thicknesses of two magnetic layers need to follow the relation: $t_1 M_1^s = t_2 M_2^s$, where t_1 , t_2, M^s_1 and M^s_2 are the thicknesses and magnetizations of two magnetic layers, respectively. The ratio between the thickness and the diameter need to be kept below 1:3 to force the magnetization stay in the film plane (a shape anisotropic effect). Also, it is critical to have magnetizations in both layers to point to the opposite direction. This requires two magnetic disks are single domain particles, which are strongly dependent on dimensions and morphologies. In a single domain element, the direction of the magnetization is determined by magnetic anisotropies, including magnetocrystalline anisotropy and shape anisotropy. At least one magnetic layer needs to be made from a magnetic material with low magnetocrystalline anisotropy (soft magnetic material), so that the minimization of magnetostatic energy can easily overcome magnetocrystalline anisotropy to force its magnetizations to point to the opposite direction of another layer. Permalloy (Ni 81% Fe19%) is widely used soft materials whose magnetocrystalline anisotropy is near zero. It has a relatively high saturation magnetization of 800 emu/cm^3. It is also corrosion-resistant. Permalloy thin films obtained using physical vapor deposition and electrodeposition are well studied. With all these properties, permalloy can be chosen as the material for “soft layer”. The choice of materials for another magnetic layer, called as “hard layer”, will be one of the determining factors for tuning saturation fields, the key for magnetic multiplexing. For nanodisks with an elongated (rectangular or elliptical) shape, the direction of magnetization is primarily determined by shape anisotropy. At remanence, magnetizations relax back to the long axis direction and two magnetizations point to

the opposite direction to minimize magnetostatic energy. This alignment to the long axis makes it possible to choose relatively harder materials as soft layer, since shape anisotropy helps to rotate the magnetization.

Saturation field

Saturation field is dependent relative orientation between magnetic moment direction and the applied field direction. First, considering the magnetic moment direction is along the applied field direction, as shown in Figure 3.4. There are two possibilities in this case: either the hard layer or the soft layer is parallel to the applied field direction. For one single layer disk, the field needed to switching the magnetization from one direction to the opposite direction is called switching field, which is dependent on anisotropy strength. For the soft permalloy layer, anisotropy is near to zero, so soft layer switching field, H_{soft}, will be very small, and can be neglected. For the hard layer, H_{hard} depends on the choice of material; it can be very large for materials with high magnetocrystalline anisotropy such as Co. The interaction between two magnetic layers can be considered as an field exerted from one layer to another layer, termed as interaction field, H_{inter}. In the case of hard layer parallel to the applied field direction, the saturation field $H_s = H_{soft} + H_{inter} = H_{inter}$. In the case of soft layer parallel to the applied field direction, the saturation field $H_s = H_{hard} + H_{inter}$. The interaction field, H_{inter}, is determined by the separation spacing, the thickness of the non-magnetic layer. The interaction can be considered as the interaction between two magnetic dipoles, whose strength is inversely propositional to cube of the separation, i.e., a small decrease of the separation will greatly increase the interaction strength, therefore the saturation field.

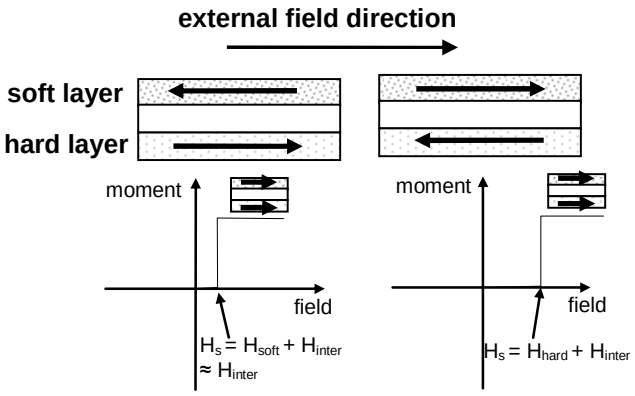

Figure 3.4 Different saturation fields results from different orientations between the magnetic moment direction and the applied field direction.

This analysis is only valid when the applied external field is along the magnetization direction. But for bioseperation, nanodisks in solution orient randomly. The magnetization from each layer lays in-plane and antiparallel to each other. If two magnetic moments from two layers are exactly the same, the net moment will be zero, and the orientation of these multilayered nanodisks will be completely random. However, it is almost impossible to get an exact zero net magnetic moment. A small net moment is always expected. A magnetic moment, *m*, oriented in a uniform field, *H*, with θ degree to the field will experience a torque: $\tau = m H \sin\theta$ will be exerted to the nanodisks and the direction of this torque is to align magnetization toward the field direction. This torque is very large even for a small moment. For example, a magnet with a very small moment of 0.001fAm^2 (10^{-18}Am^2) in a 0.01T (100 Oe) field with θ = 90º, the torque is 0.00001 fNm. If the diameter of the disk is 50 nm, the equivalent force on the edge of the disk is 0.00001fNm/ 25 nm = 0.4 pN, which is a large force to a nanoparticle, much more than enough to rotate the disk in the field direction. According to this analysis, inside the solution, nanodisks are expected to align the magnetization with applied field direction in solution, as shown in Figure

3.5. Whether the soft layer or hard layer is parallel to the field direction is determined by which layer has a larger moment. To know exact saturation field of nanodisks in solution, we can intentionally make the moment in one layer slightly larger than another layer, which will make the nanodisks to have a small net moment.

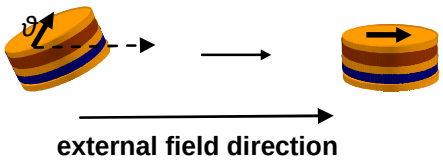

Figure 3.5 Nanodisk with a small net moment in a uniform field will rotate to align its moment with the field direction.

Tuning saturation field can be summarized as the follows: If the moment of soft layer is larger, the saturation field can be tuned by adjusting spacing layer thickness, and the material choice for hard layer has little effect on saturation field. If the moment of hard layer is larger, the saturation field is controlled by spacing layer thickness and the material choice for hard layer. With the tunability of saturation field, multilayered nanodisks with similar dimensions can possess very different saturation fields, which is the basis for “magnetic multiplexing”. For example, considering two kinds of magnetic nanoparticles with different saturation fields, under a certain applied magnetic field, one kind of nanodisks can be strong magnets and the other kind of nanodisks are nonmagnetic or very weakly magnetic. Accordingly, magnetic force exerted from a field gradient and the extent of the deflection will be totally different for these two kinds of nanodisks.

3.1.3. Selection of materials

One magnetic soft layer and one magnetic hard layer are used in this design. The requirement for magnetic soft layer is magnetic material having low magnetocrytalline anisotropy. Permalloy ($Ni_{81}Fe_{19}$) has been extensively used as soft magnetic material because the magnetocrystalline anisotropy is near zero. Also, permalloy has fairly high magnetization of 800 emu/cm^3 and it is corrosion-resistant. The soft magnetic layer is easily rotated in the opposite direction of the hard layer. The hard layer in this design is cobalt (Co) because of its high magnetocrystalline anisotropy which makes it difficult to switch magnetization. Cobalt has extremely high magnetization of 1400 emu/cm^3. Permalloy and cobalt thin film can be easily fabricated using physical vapor deposition. With these properties, permalloy and cobalt are the first candidate for soft and hard layer, respectively.

3.1.4. Size and thickness

The size of nanodisks determines saturation moment, and also determines sensitivity to utilize in particular application such as DNA microarrays. The important factor of the size is that either magnetic moment is weak or strong to be detected. For example, a nanodisk, as shown in Figure 3.6, with a diameter of 80 nm, and thickness of soft layer Nife 18 nm and hard layer Co 10 nm is calculated as 0.14 pico-emu. This magnetic moment can be detected by magnetoresistive sensor.

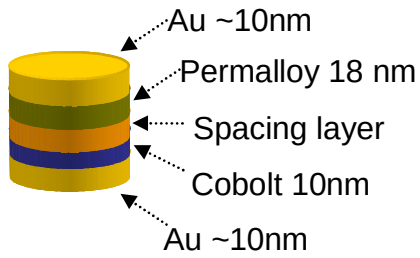

Figure 3.6 Configurations of single stack of multilayered magnetic nanodisk.

An important parameter is that the ratio between thickness and diameter of the magnetic layer has to be below 1:3 to force magnetization to point the in-plane direction [42]. Also, these two magnetic layers must be single domain particles in order to have magnetizations in both layers point to the opposite direction.

3.2. Granular magnetic Au nanodisks

Formation of metal layer using either electrodeposition or evaporation starts from islands. If the growth process stops at the early stage, we will obtain a structure with magnetic islands embedded inside gold matrix, and these ialands are small enough to be superparamagnetic. The magnetic moment from a single layer of islands is too low, then by depositing many layers of gold and magnetic alternating layers, the entire particle can have a large moment with zero remanence. In this design, this particle will combine both magnetic and optical properties in one nanoentity.

The schematic of granular magnetic gold nanodisk is shown in Figure 3.7. The magnetization of a superparamagnetic nanoparticle flips its direction in the absence of the applied field due to the thermal energy. If an external field is applied, the magnetization tends to align to the field direction, at the same time, thermal energy still tends to randomize the magnetization. These characteristics of a superparamagnetic nanoparticle make it non-magnetic without external field (no remanence), which can avoid the aggregation of particles due to magnetic attraction, strongly magnetic when an external field (saturation field) is applied. In this configuration, superparamagnetic nanoparticles are encapsulated in a gold matrix, which can protect metallic magnetic materials from oxidation. The particles have a

disk shape with flat surfaces, which is suitable for bioapplications such as labels for magnetoresistive sensors. The expected hysteresis loop is shown in Figure 3.8.

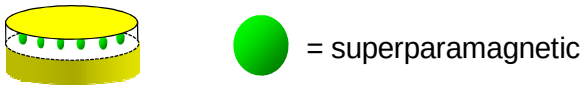

Figure 3.7 Configuration of the granular superparamagnetic embedded in nanodisk.

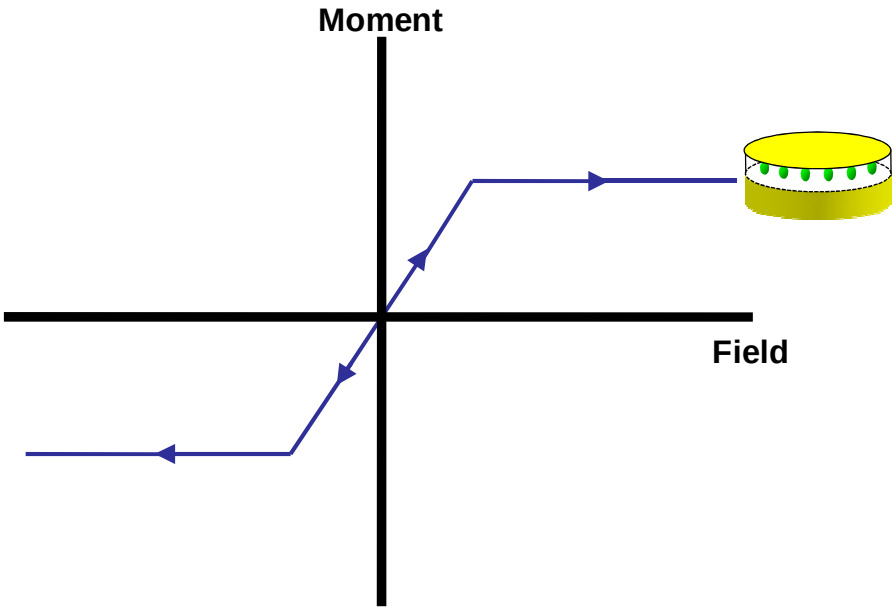

Figure 3.8 Expected hysteresis loop of the granular superparamagnetic embedded in nanodisk.

3.2.1. Increasing magnetic moment

The magnetic moment from a single layer of superparamagnetic nanoparticle is too low. The entire particle has a magnetic moment $\mu = nM_sV$, where n is the number of particle in that layer. To generate well dispersed islands, the thickness of the magnetic layer must be very thin (< 2 nm), which has very small amount of magnetic material. To further increase the moment, several magnetic layers separated by gold can be stack together to form rod-like structure and the magnetic moment of the entire particle increases to $\mu = nxM_sV$, where x is the number of

stacked layers. In summary, each superparamagnetic island in the particle will be seperated by Au, generating a structure with metallic magnetic nanoparticles embedded in Au. Therefore, high saturation magnetic moment and zero remanence are achieved, as shown in the hysteresis loop in Figure 3.9.

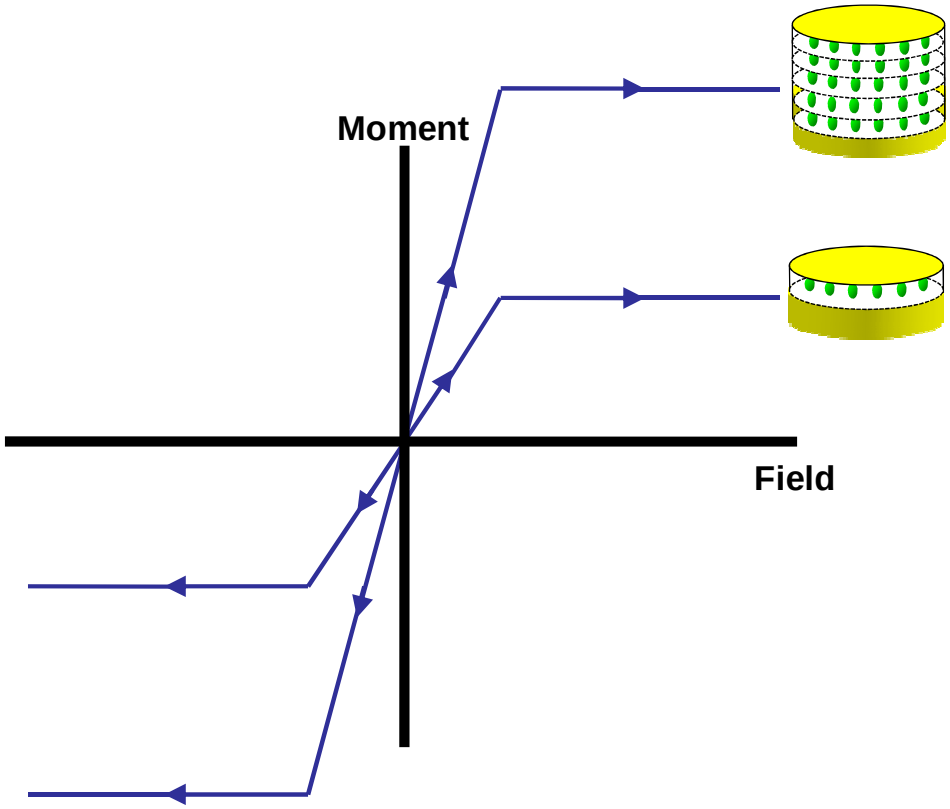

Figure 3.9 Expected hysteresis loop of the granular superparamagnetic embedded in nanodisk with several layers.

3.2.2. Tuning magnetic properties

The magnetic properties of granular magnetic Au nanoparticles can be tuned by using different magnetic materials for different layers. Since the gold matrix contains several layers of magnetic material, difference materials can be used for different layers. In this case, nanoparticles can exhibit strongly or weakly magnetic depending on different applied external fields, as shown in Figure 3.10.

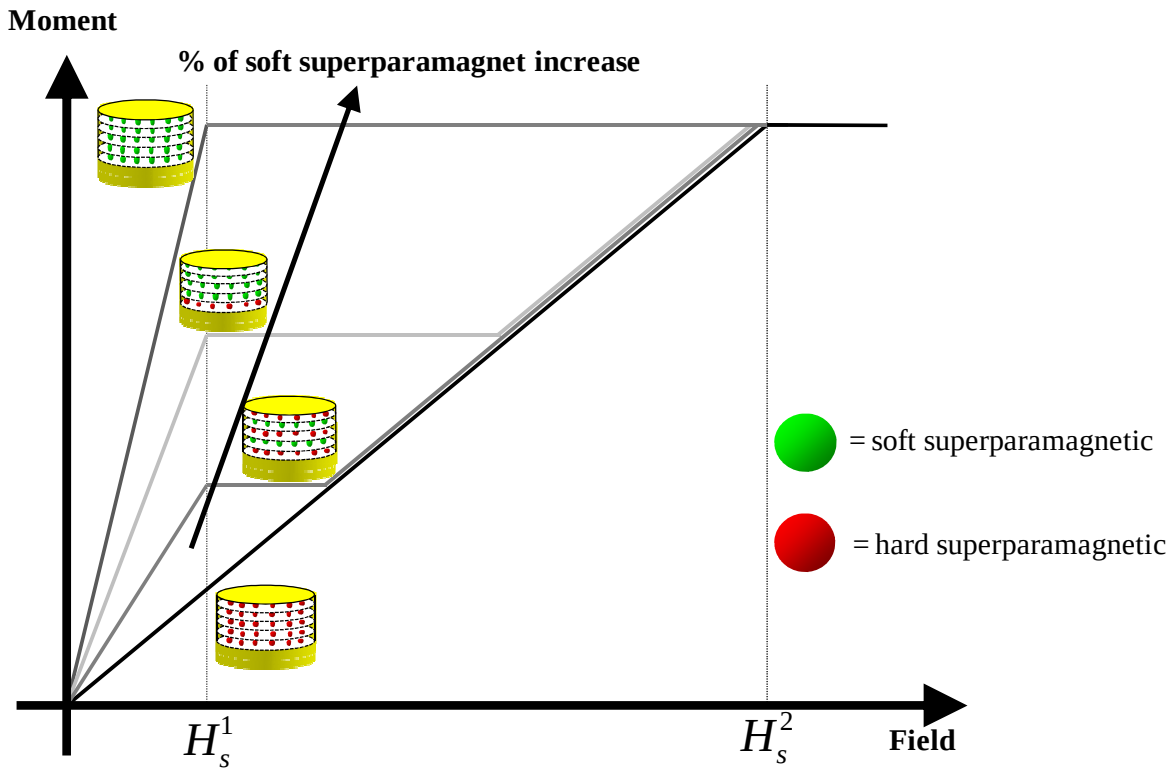

Figure 3.10 Tunability nanodisks with different saturation fields.

Magnetocrystalline anisotropy is a property of each material. Soft magnetic has a low magnetocrystalline anisotropy, which requires a low applied field to saturate magnetic moment. Soft superparamagnetic nanoparticles requires the applied magnetic field, H_s^1, to align magnetization in parallel direction. Above the field of H_s^1, the layers containing of all soft superparamagnetic particles behave as a strong magnet. On the other hand, all hard superparamagnetic particles show only a weak magnetic behavior. Above the field of H_s^2, both soft and hard superparamagnetic nanoparticles become strong magnets.

3.2.3. Selection of materials

Any magnetic material can be used in this design, but the island size must be in superparamagnetic range. The soft magnetic material is desirable because only low external applied field is needed to obtain a large moment, which is desirable for bioapplications. Permalloy ($Ni_{81}Fe_{19}$) is the first choice as soft magnetic material because of its near zero magnetocrystal anisotropy. However, for evaporation and electrodeposition, the deposition of alloy with precise composition can be difficult. In this case, single element materials such as iron (Fe), nickel (Ni), or cobalt (Co) can be used. Iron has a very high magnetization of 1700 emu/cm^3 and is biocompatible. Also, the magnetocrystalline anisotropy of iron is not too high. Nickel can be also chosen because of its corrosion-resistant and lower magnetocrystalline anisotropy, which is lower than cobalt and iron. Nickel has a magnetization of 480 emu/cm^3 which is much lower than Fe and Co. Cobalt has a very high magnetocrystalline anisotropy. All single magnetic elements can be easily fabricated using physical vapor deposition.

A matrix is used to separate magnetic nanoparticles and protect them from oxidation. Also, it needs to be biocompatible for bioapplications. Gold and silicon oxide are two inorganic materials widely used for bioapplications. Gold is chosen here since gold nanoparticles with a proper size scale also have special optical properties and are useful in biology and medicine. Gold nanoparticles exhibit surface plasmon resonance (SPR) effect. SPR is a nanoscale size effect of the interaction of an electromagnetic wave with the conduction electrons in a metal. When a metal is under the irradiation of light, the electric field drives the conduction electrons to oscillate. This collective motion of electrons has its resonance

frequency, plasma frequency, and the quanta of this collective oscillation are called plasmons. When dimensions (at least one) of the metal is much smaller than the wavelength of the light, this collective excitation mode of the plasma will be localized near the surface, and the resonant frequency will shift from the ordinary plasma frequency to surface plasmon resonance (SPR) frequency. The SPR frequencies lie in visible light range for Cu, Ag and Au nanoparticles. The incident light at SPR frequency is strongly absorbed by these metal nanoparticles, giving them intense colors and other interesting optical properties. Some of the absorbed photons will be released with the same frequency in all directions, which is known as scattering; some photons will be converted into phonons, which are referred to as absorption. The SPR frequency and cross-section of SPR scattering and absorption are dependent on the size and shape of nanoparticles, inter-particle interactions and dielectric properties of the surrounding medium.

3.2.4. Size and thickness

The size of magnetic nanoparticles determines magnetic properties. In this design, thickness of each magnetic layer must be very small to maintain superparamagnetic state. The critical sizes at which superparamagnetic state occurs at room temperature are estimated as 7 nm for Co and 6 nm for Fe. To increase magnetic moment, several layers stack together For example, a nanodisk, shown in Figure 3.11, has a diameter of 3 nm Fe nanoparticles embedded in gold matrix. The entire particle has a diameter of 80 nm and 5 magnetic layers. The volumetric percentage of embedded magnetic nanoparticles is about 20%. The calculated magnetic moment of each particle is 0.03 pico-emu.

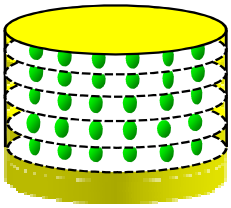

Figure 3.11 Configurations of several stacks of superparamagnetic embedded in nanodisk.

The size of the entire paticle effects its optical properties. There are two types of surface plasmon resonances; transverse oscillation of the electrons, which is around 520 nm, and longitudinal plasmon resonance which is at a longer wavelength. Varying aspect ratio of gold matrix from nanodisk to nanorods affects only the longitudinal surface resonance. Larger aspect ratio increases the longitudinal surface plasmon resonance, shifting to longer wavelength.

CHAPTER 4

EXPERIMENTAL METHODS

In this study, the experimental methods include three parts; thin film preparation and magnetic property characterization.

4.1. Thin metal film preparation

Physical vapor deposition, evaporation and sputtering, and electrodeposition are used to deposit metal films.

Evaporation

The evaporation system consists of an evaporation source and a substrate holder in a vacuum chamber. The evaporation source is used to vaporize the desired material and a substrate is located at a proper distance facing to the evaporation source.. The substrate can be heated or rotated during deposition. The evaporation system is shown in Figure 4.1.

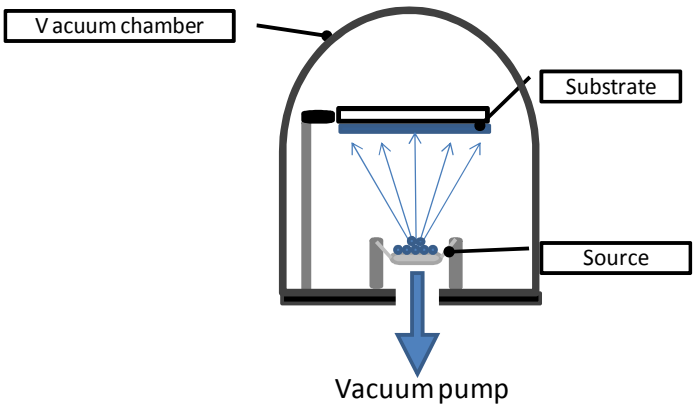

Figure 4.1 Schematic drawing of the evaporation system.

The materials can be deposited by heating the source at the elevated temperature; using either resistance heater (thermal evaporator), electron-beam (e-beam evaporator) or laser (pulse laser deposition). We use thermal and e-beam evaporator to deposit Al, Cu, Ni, Au, and Fe. The experimental conditions are listed in Table 4.1.

Table 4.1 Conditions used for evaporation process.

Evaporation method	material	base pressure	evaporation rate
Thermal	Au	5×10^{-6}	0.3 A°/s
	Cu	5×10^{-6}	2-3 A°/s
	Al	5×10^{-6}	1-1.5 A°/s
E-beam	Ni	3×10^{-6}	0.5 A°/s
	Fe	3×10^{-6}	0.5 A°/s
	Au	3×10^{-6}	0.3 A°/s
	Al	3×10^{-6}	1-1.5 A°/s

Sputtering

A typical sputtering system is shown in Figure 4.2. Sputtering is the technique that uses high energy of ions to knock atoms out from a target to deposit them onto the substrate. The target serves as one electrode and the substrate acts as another electrode. An inert gas such as argon with a pressure around 5-100 mtorr is introduced into the system. When DC is applied to the electrodes, a glow discharge is occurred between two electrodes. Free electrons are accelerated by the electric field and gain energy to ionize argon atoms to become argon positive ions, Ar^+, as shown below.

$$e^- + Ar \rightarrow Ar^+ + 2e^-$$

The Ar^+ knocks atom out from a target resulting in the ejection of neutral target atom through momentum transfer. The ejected atoms deposit on the opposite electrode.

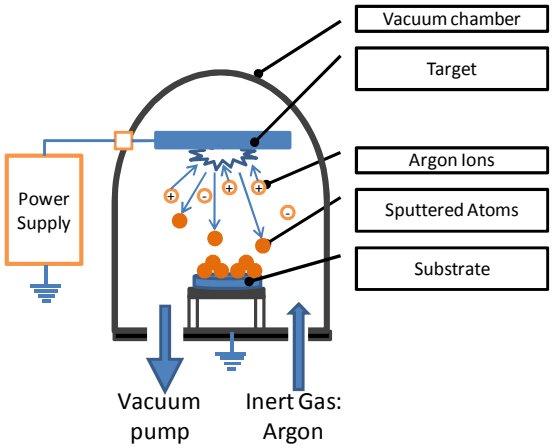

Figure 4.2 Schematic drawing of sputtering.

Table 4.2 Conditions used for sputter deposition of different metals.

Sputtering	material	base pressure (torr)	Argon pressure (torr)	Power (w)	Sputtering rate
from NMMRG lab	Ag	5×10^{-6}	5×10^{-3}	120	3 A⁰/s
	Cu	5×10^{-6}	5×10^{-3}	120	3 A⁰/s
	NiFe	5×10^{-6}	2.5×10^{-3}	40	0.2 A⁰/s
	Co	5×10^{-6}	2.5×10^{-3}	40	0.2 A⁰/s
from SaNEL lab	Al	5×10^{-6}	5×10^{-3}	100	0.3 A⁰/s

Electrodeposition

Electrodeposition is to reduce cations of a desired material by using external electrical power.. When a metallic salt is dissolves in water, it can form positive ions in solution. The solution that contains these charged ions is referred to as an electrolyte.. The reaction is expressed as.

$$M^{n+} + ne^- \rightarrow M$$

The thickness of the deposited material using electrodeposition is controlled by the total charge passed.The experimental setup for the electrodeposition process is shown in Figure 4.3. A standard three electrode electrochemical cell with a saturated Ag/AgCl electrode as reference electrode and 99.99% pure platinum mesh as the counter electrode was used.

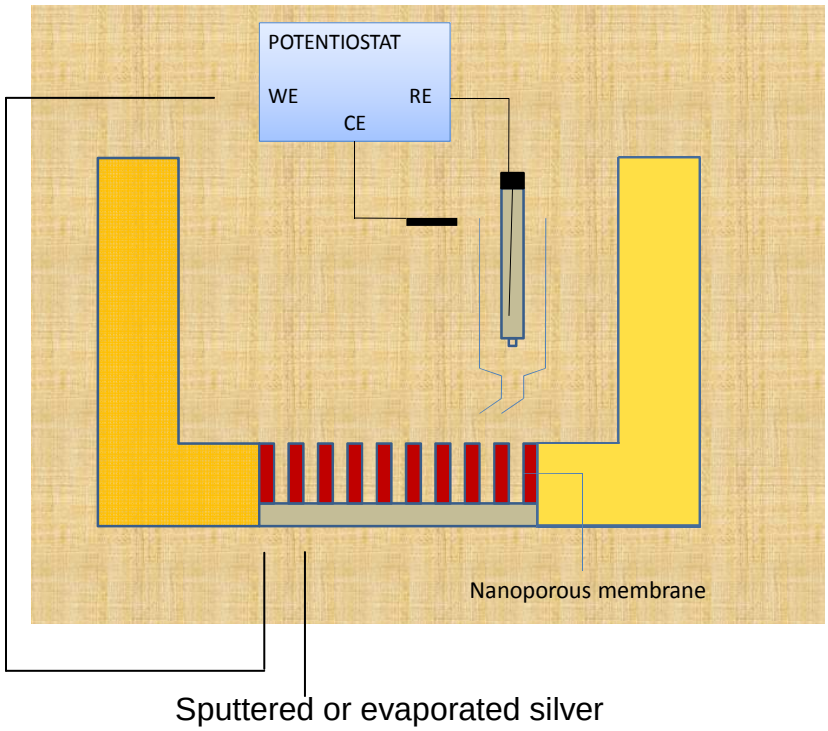

Figure 4.3 Schematic drawing of electrodeposition process.

4.2. Magnetic property measurements

Magnetic material in a uniform magnetic field produces a distortion of the field, which affects the flex distribution and is detected by an inductive coil. This is the fundamental basic for magnetometers.

4.2.1. Vibrating sample magnetometer (VSM)

VSM method is based on the change of the magnetic flux in a coil when a magnetic sample is vibrated during measurement. A typical VSM is shown in Figure 4.4. The sample is placed at this end of the glass rod, the electromagnet produces a uniform field to magnetize the sample between two poles, the pick up coils are located at the electromagnet to avoid vibration of the coils with respect to the magnet.

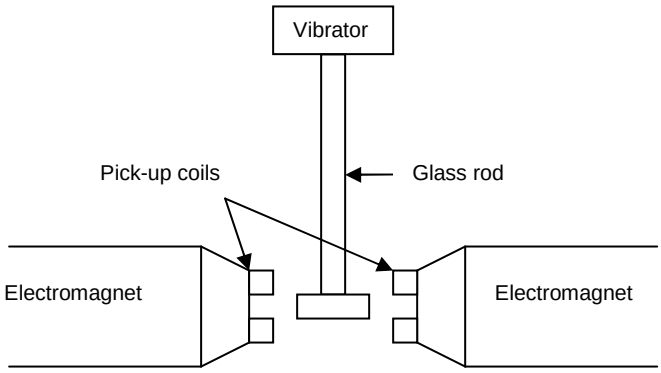

Figure 4.4 Schematic drawing of a vibrating sample magnetometer.

The sample is vibrated near a pick-up coil, and the magnetic flux change is detected, which is proportional to the magnetic moment of the sample. The sample is vibrated during the measurement at small amplitude with a frequency around 70 Hz, which produces a field distortion. A pick-up coil can detect this field distortion and then the field distortion is converted with conventional processing equipment. The magnetic moment from sample is followed Faraday law of induction, namely a potential drop V. A potential drop is induced across the pick-up coil because of a change of flux:

$$V = -N\frac{d\phi}{dt}$$

Where N is the number of turns in the detection coils and and Ø is the flux in the coils, which is proportional to the magnetic moment of the sample. A VSM usually has a sensitivity about 10^{-6} emu.

4.2.2. Alternating gradient magnetometer (AGM)

In AGM, the sample is mounted to the end of the extension rod attached with piezoelectric element. A typical AGM is shown in Figure 4.5. The electromagnet produces a uniform field between two poles. A pair of gradient coils are mounted to the electromagnet and generate an alternating gradient field.

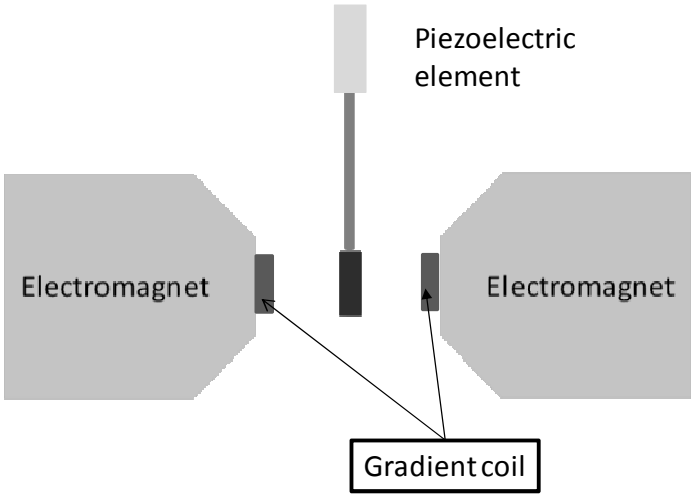

Figure 4.5 Schematic drawing of an Alternating gradient magnetometer.

The sample is magnetized by a uniform field from the electromagnet during the measurement. Simultaneously, the sample is also subjected to an alternating field gradient that produces an alternating force on the cantilever. The force is proportional to the magnitude of the gradient field and the magnetic moment of the sample.

$$F_x = M_x \frac{dH}{dx}$$

Where F_x is the force, M_x is the magnetic moment, and $\frac{dH}{dx}$ is the gradient field. The deflection of the cantilever from this force is proportional to the voltage output of the piezoelectric element, which is also detected at the operating frequency of the gradient field. The system determines the mechanical resonance and sets the appropriate operating frequency. Therefore, the amplitude of the voltage is proportional to the magnetic moment of the sample. The signal developed by the piezoelectric element is enhanced by operating at or near the mechanical resonant frequency of the assembly. The AGM in this study has a a sensitivity of about 10^{-6} emu and the maximum field from electromagnet is about 15000 Oe.

CHAPTER 5

GENERATION OF ULTRA THIN ANODIZED ALUMINA TEMPLATE

Using evaporation deposition method to generate nanoparticles inside a hole template offers two important advantages: 1) It greatly increases the possible combination of materials since almost all materials can be evaporation deposited. This is particularly important for our multilayered structures which involve several different materials. 2). Evaporation allows the precise control of the layer thickness and the interface between layers. However, the hole template for evaporation must be ultra-thin so that the materials can go to the substrate. For this purpose, we developed an ultrathin AAO template on Si substrate. In this chapter, this template generation process is discussed. First, the fundamentals on anodization of aluminum is given.. Then, the conditions and experiment results of the anodization of untra thin aluminum films are described. Finally, the effects of template generation parameters on morphology of nanodisks are discussed.

5.1. Introduction of anodization of aluminum

Prior to the discussions of anodization of aluminum, the basic of physical and chemical properties of aluminum are given as background knowledge. Aluminum is a soft metal with durable and lightweight characteristics. The structure of aluminum is a face centered cubic structure. The oxidation state of aluminum exists from +1 to +3 but state +3 is common. The melting temperature of aluminum is at 660˚C. Metallic aluminum is very reactive with oxygen, causing aluminum oxide formation. Aluminum

oxide is a ceramic material and is an electrical insulator. The aluminum oxide formed from atmospheric oxygen naturally occurs in a very thin oxide layer form. The thickness of aluminum oxide can be increased using a process called anodization. The anodization process is a process where the reaction takes place at the anode electrode of electrical circuit. The aluminum oxide generated by anodization process is usually amorphous. The aluminum oxide from anodization process generates two film types; barrier type and porous type films, depending on the electrolyte and applied voltage.The barrier type oxide layer is formed when aluminum is anodized in weak acids such as neutral boric acid solution and citric acid at pH value 5-7. The as-formed oxide layer in this type is completely insoluble. For porous type, metallic aluminum must be anodized in the acids in which the as-form oxide is slightly soluble. Several electrolytes can be used to form porous aluminum oxide, such as sulfuric, phosphoric, chromic, oxalic acids at almost any concentration. By adjusting anodization conditions, uniform porous aluminum oxide can be formed.

The oxide growth of an anodization process to produce porous aluminum oxide is quite complicated. This process involves an electric field at the interfaces which influences the reaction. Generally, types of electrolyte, the temperature of the electrolyte, the thickness of aluminum, the separation between electrodes, and the applied voltage all affect the formation process of porous anodic porous alumina.

In this study, anodization process is done in a glass cylindrical cell. The distance between electrode and counter electrode is kept at a constant 1 cm and the surface area of aluminum exposes to electrolyte is around 0.55π cm^2. The amount of exposed aluminum affects the current density; more aluminum surface area that exposes to electrolyte leads to less current. Also, the distance of two electrodes

affects the strength of electric field. For the counter electrode, several materials can be used such as C, Ag, or Au. In our set up, Pt mesh is used. The anodization process can be conducted using either constant current or constant voltage. A constant DC voltage is applied in this study. The set-up for anodization of aluminum is shown in Figure 5.1.

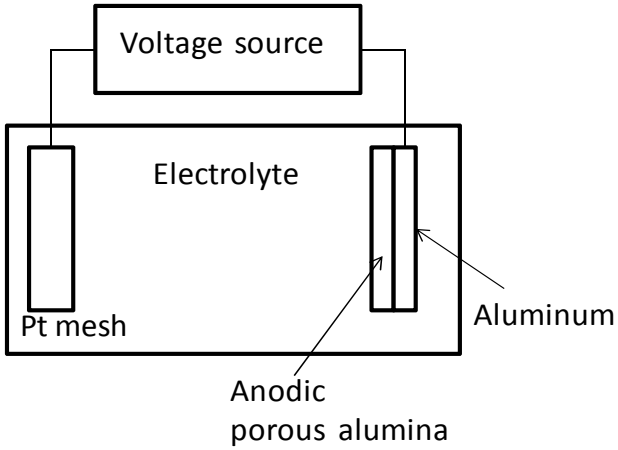

Figure 5.1 Schematic drawing of a setup of anodization process.

Compared to growth mechanism, the experiment of anodization process to produce porous aluminum oxide is simple. There are two ways to fabricate porous aluminum oxide; 1-step or 2-step anodization. In 1-step anodization, aluminum piece is placed in a cell, an electrolyte is poured into the cell to cover the aluminum surface, and then a constant voltage is applied. The resulting porous aluminum oxide is removed and washed. 2-step process is usually employed for aluminum foil or thick aluminum film, aiming to obtain better ordered structures. Similar to 1-step process, aluminum is first anodized. Then, the anodized oxide layer is etched using mixture of chromic acid and phosphoric acid. The remaining part is only aluminum with U-shaped structures on the top of the surface. The sample is re-placed in the cell and re-anodized. In 2- step process, the obtained structure is always better than

1-step process. However, in our study, 2-step anodization cannot be employed because the aluminum film is very thin.

Currently, high throughput, low cost, and highly controllable anodization of aluminum procwss has been developed. Nanoporous anodic alumina oxide (AAO) has been extensively used as templates for synthesis of nanorods, nanotubes and nanowires. Porous alumina with cylindrical pores of variable diameter sizes from a few nanometers to several hundreds of nanometers and thickness from several micrometers to over 100 micrometers has been developed. However, anodization of ultrathin aluminum has not been reported.

5.2. Results and discussions

5.2.1. Aluminum film deposition

The preparation of aluminum films is very important for anodization process. Deposited aluminum film should have a mirror-like smooth surface. The aluminum films have been deposited using sputtering and evaporation. Top surfaces of aluminum films on Si substrate using sputtering or evaporation is shown in the Figure 5.2.

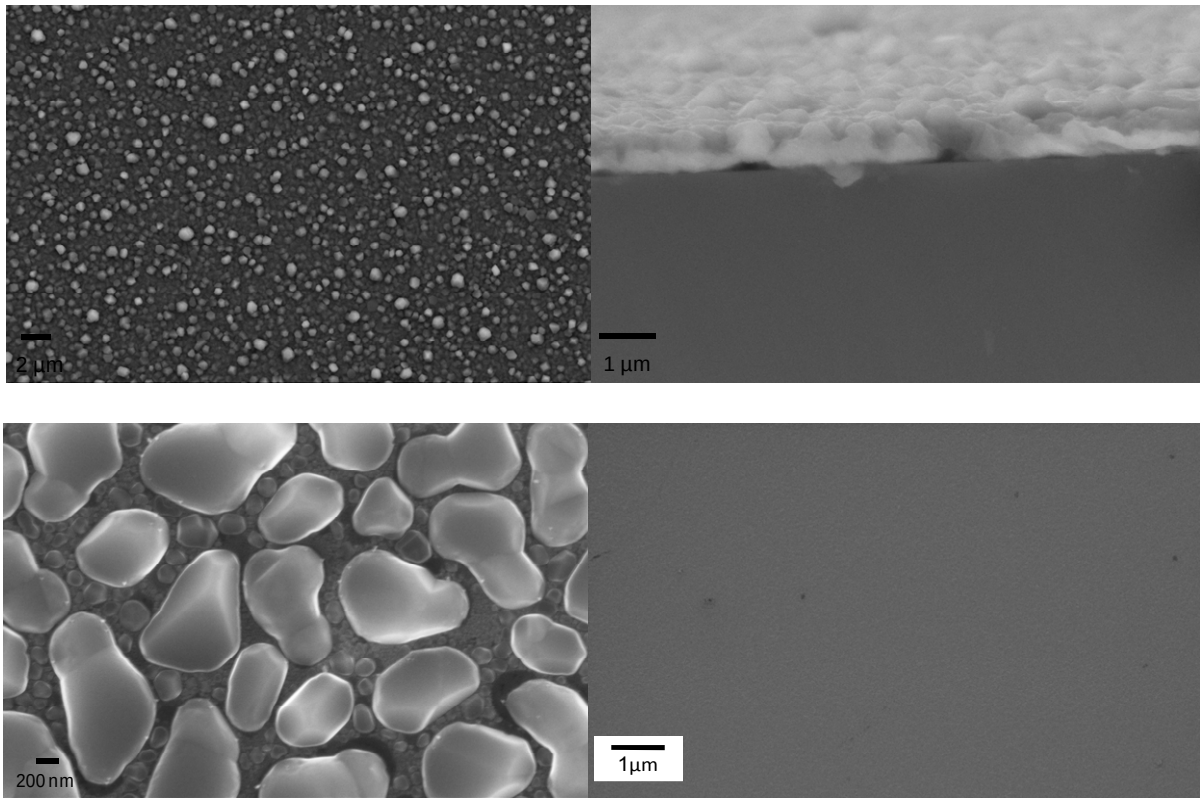

Figure 5.2 SEM micrograghs of aluminum film deposited using sputtering(top) at room temperature, at elevated temperature (bottom, left), and using evaporation (bottom, right)

The surface of sputter-deposited aluminum film is rough. An annealing process did not improve the quality of aluminum film,. Evaporation deposited film (with a base pressure of 5×10^{-6} Torr) gives the best results, and is used in the subsequent anodization steps.

5.2.2. Conditions used for anodization process

We chose oxalic acid electrolyte in our study since the expected pore diameter is relatively large and the anodization process can be controlled easier than using phospholic acid. It is known that anodization using sulfuric acid results in smaller diameters which may become a problem when porous alumninum is used as

template for evaporation. In our experiments, the single step anodization is conducated in 0.23 M oxalic acid at 25 ˚C.

Effect of applied voltage

Pure aluminum films with the thickness of 100 nm are deposited onto Si substrate using evaporation at a rate 1-1.5 nm/s. An effect of applied voltage is studied to find the right condition of anodization process. All the parameters of experiments are kept in the same condition; except voltage. The electrolyte is 0.23 M oxalic acid. Anodization time is 30 seconds. The anodization is conducted at room temperature. The results are shown in Figure 5.3.

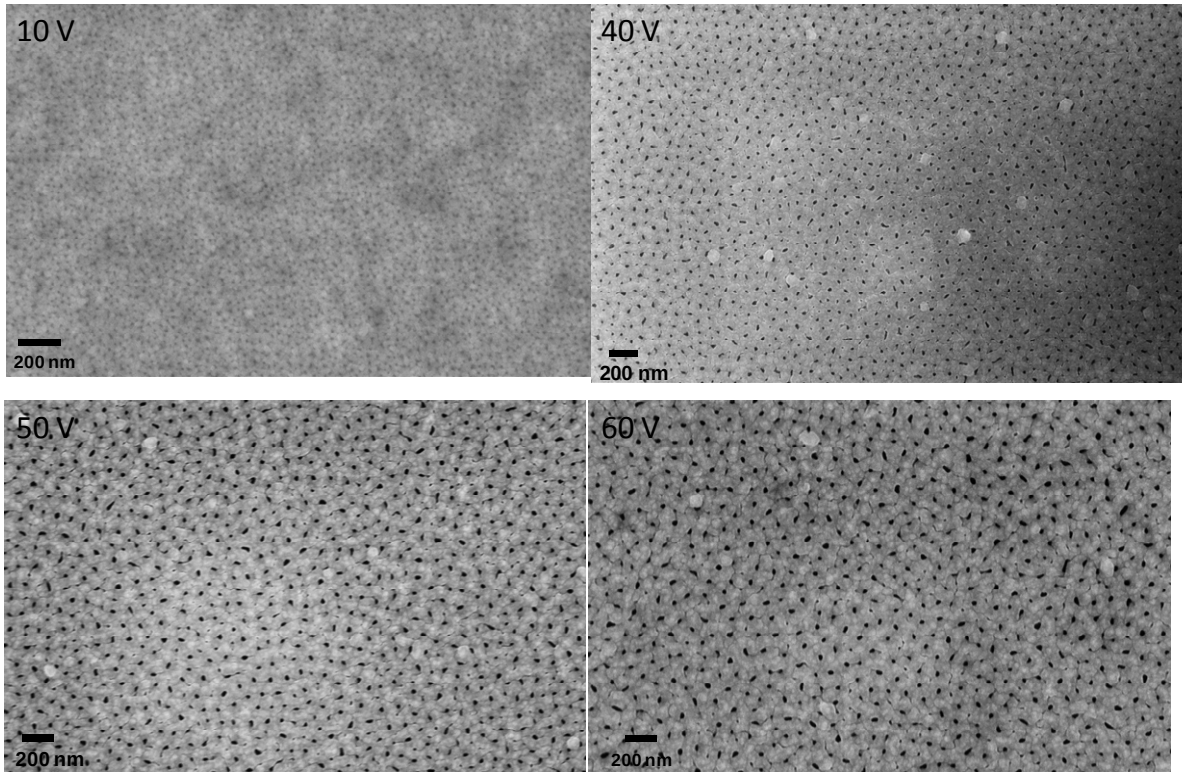

Figure 5.3 SEM micrographs of pores formed by anodization at 10, 40, 50, and 60V with 0.23M oxalic acid.

Pore nucleation starts to occur at low voltage such as 10V and happens almost at the same time as the aluminum oxide growth. Pore growth is due to field-

assisted hydrogen ions attacking on the oxide layer. At this point, the surface shows only many small pits not pores because applied voltage is small so that field-assisted hydrogen is not suffucient to produce pore. With increasing voltage, pore channels grow and the pore size increases. At higher voltage, 40 to 60 V, pores are first formed at pits where the electric field is concentrated after the formation of barrier layer. Then, the pore is grown in the direction perpendicular to surface with field-assisted hydrogen ion at the oxide/electrolyte interface and oxide growth at the metal/oxide interface. In anodization process, the temperature rises up because the reaction is exothermic. The heat generated from anodization create a localized temperature increase. Increasing voltage also increases temperature to the reaction.

The lateral growth of pore during anodization process is also observaed and increased with applied voltage, which is indicated in the pore diameter. The pore diamter increases with anodization voltage. In this process, the repulsive interaction between the pore drives the structural adjustment to form periodic hexagonal pore structure. However, the uniformity of pores decreases with applied voltage Increasing voltage, the pore growth in the direction perpendicular to the surface increases because the migration of cations and anions is faster. The larger migration velocity leads to the thickening of the porous aluminum oxide and increase of lateral growth, causing the increase of pore diameter and spacing. The adjustment velocity among the pores cannot keep up with the growth velocity of porous aluminum oxide, so that the quality of the ordering of porous aluminum oxide decreases. In this case, 40V is the optimum condition to produce porous aluminum oxide.

The number of pores is not only relied on the voltage but also depends on the electrolyte, the local field, and cation-anion content, as well as a quality of aluminum film sample.

Effect of the thickness of aluminum film

The thickness of aluminum films affects pore structure, especially the barrier layer at the bottom. Aluminum films with different thicknesses, 150 nm and 1 micron, are deposited on silicon substrate. After anodization, both sample are immersed into 5% phosphoric acid for a period of 40 min. The results are shown in Figure 5.4.

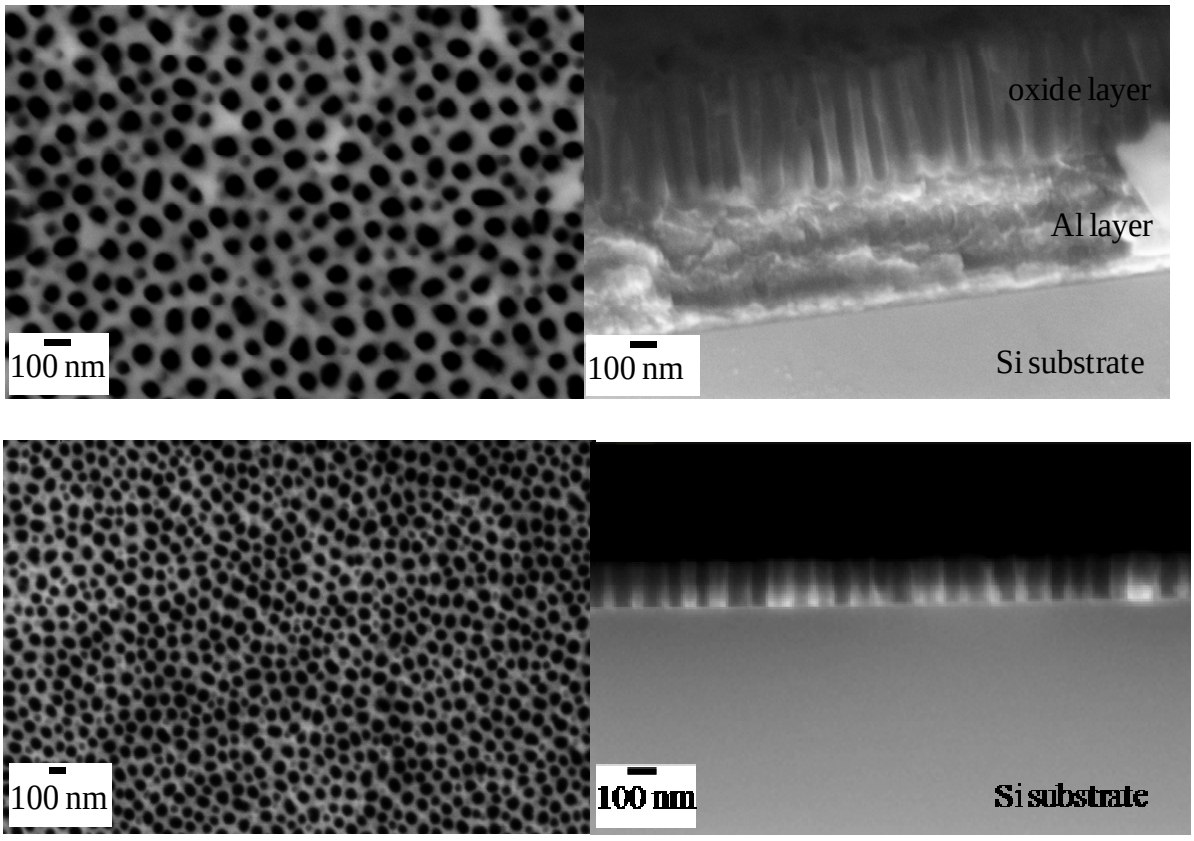

Figure 5.4 SEM micrographs of pores formed by anodization 40V thick film (top) and thin film (bottom).

The thickness of porous aluminum oxide is about 500 nm in 1 micron thick aluminum film, the anodized porous aluminum oxide with straight pore length is

about 500 nm. After dipping into phosphoric acid for a period of 40 min, U-shape oxide barrier layer at the bottom of the pores is clearly seen. The ordering of thick film is better than thin film because pores can be arranged during anodization. A thick film allows pores to form ordered structures, whereas in a thin film pores do not have enough time to rearrange (illustrated in Figure 5.5). However, the ordering and uniformity of pores from 100 nm aluminum oxide film are fairly adequate for our purpose of the fabrication of nanoparticles.

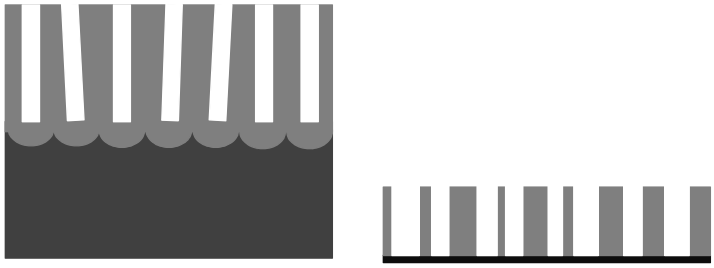

Figure 5.5 Schematic drawing of pore arrangement during anodization.

The thickness of aluminum films is very important for nanoparticles fabrication. The effect of aluminum films thickness on the morphology of nanoparticles produced is studied. All parameters are kept the same, except the thickness of aluminum films. The anodization process ends at the lowest current point. Cr/Au with thickness 30/50 Aº is evaporated into the templates. The shape of nanoparticles fabricated with different aluminum film thickness is shown in the following micrographs.

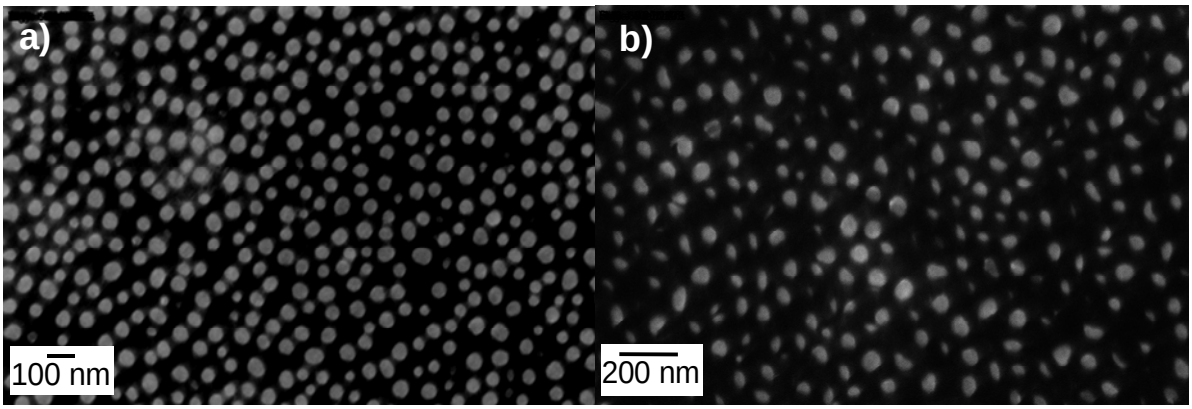

Figure 5.6 SEM micrographs of Cr/Au 30/50 Aº nanodisks produced by a) 150 nm and b) 300 nm alumina template.

Using the thinner (100 nm) template (hole aspect ratio is about 3:1) well defined disks can be generated. For higher aspect ratio holes, due to the shadowing effect, it is very difficult to have well-defined disks. Moreover, as mentioned before, during anodization process, pores try to arrange themselves to achieve periodic structure. In thick films holes are not straight, having a small tilt angle.

Void formation underneath anodic alumina

For ultrathin AAO template, one prominent problem we face is that the AAO is prone to peel off from the Si substrate. To find out the exact reason, we studied the AAO structure at different anodization stages. About 100 nm thick Al is deposited on a Si wafer using evaporation. The film is anodized in 0.23M oxalic acid at 40V. When the anodization process ends as pores reach Si substrate, aluminum converts to porous aluminum oxide. Besides the inverted U-shape barrier layer, voids appear underneath each barrier layer (shown in Figure 5.7). This phenomenon has not been obsevered in thick aluminum foil case. The finding of these voids explains why ultra thin AAO films are so easy to peel off from the substrates. There are two possible reasons for such void formation: 1) vacancies from alumina coalesce (a special case

of Kirkendall effect [43] or localized delamination of the alumina film due to stress [44].

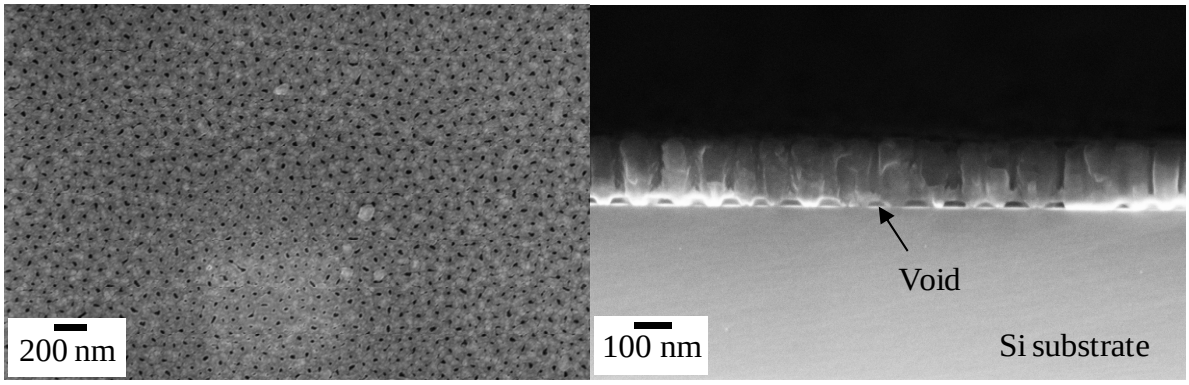

Figure 5.7 SEM micrographs of voids in anodic alumina film

It has been known for more than half a century that porosity may result from differential solid-state diffusion rates of the reactants in an alloying or oxidation reaction. In 1947, Kirkendall reported the movement of the interface between a diffusion couple, i.e., copper and zinc in brass, as the result of the different diffusion rates of these two species at an elevated temperature, which is now called the Kirkendall Effect. This was the first experimental proof that atomic diffusion occurs through vacancy exchange and not by the direct interchange of atoms. The net directional flow of matter is balanced by an opposite flow of vacancies, which can condense into pores or annihilate at dislocations. Such directional material flows also result from coupled reaction-diffusion phenomena at solid/gas or solid/liquid interfaces, leading to void formation. These voids are usually explained by outward transport of fast-moving cations through the oxide layer and a balancing inward flow of vacancies to the vicinity of the metal-oxide interface. However, the pores produced at a metal-metal diffusion couple or near the metal-oxide interface of a growing oxide do not yield monodisperse arrays of voids, but instead form a very

heterogeneous ensemble. The observed volume fraction for pores is also commonly much smaller than would be expected for the known material flows. This is because vacancies can diffuse into large volume of material and react with the large number of defects.

In the case of anodization of aluminum (oxidation of aluminum), Al^{3+} ions are generated on oxide/metal interface and migrate through oxide layer. This faster moving Al^{3+} ion flow is compensated by a vacancy flow. If large volume of metal still exists underneath anodic porous, metal acts as annihilated site to absorb these vacancies, no observable void can form. When aluminum oxide is close silicon substrate, there is not enough aluminum metal at the base to absorb all vacancies, and silicon substrate has very few annihilation sites, then vacancies coalesce into a single void. With further anodization process, the aluminum is all consumed to convert to alumina, and then we see voids underneath the alumina barrier layer, as shown in Figure 5.8.

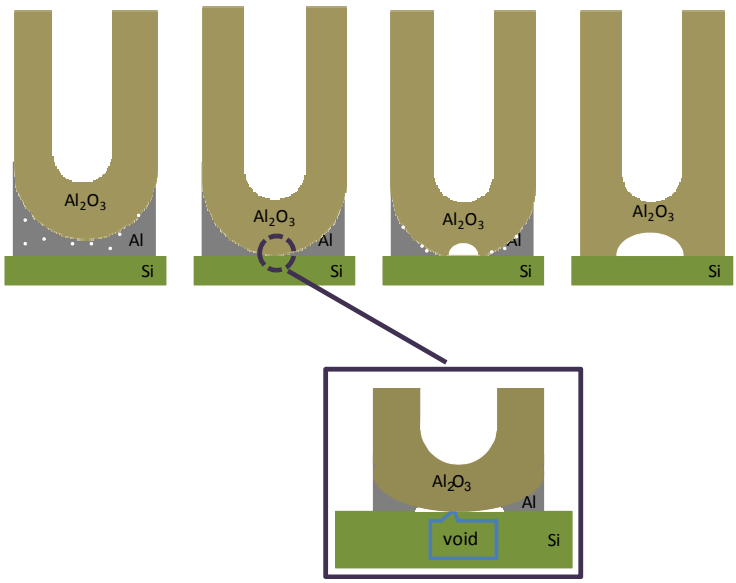

Figure 5.8 Schematic drawing of void forming during anodization.

In stress-induced localized delamination, a film that is bonded to a substrate and subjected to a compressive stress may delaminate. An interface crack can be driven by the stored elastic energy of the system which is released when the film buckles. The stress required to buckle the film is given by

$$\sigma_c = \pi^2 E\left(h/b\right)^2 \left[12\left(1-v^2\right)\right]^{-1}$$

where E is the modulus, h is an elastically isotropic film of thickness, v is the Poisson's ratio, and $2b$ is a strip of delamination of width (see Figure 5.9).

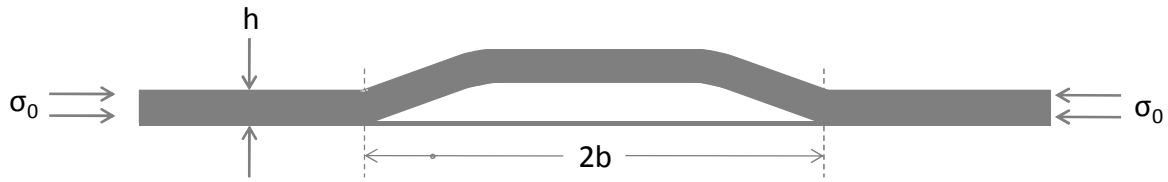

Figure 5.9 Schematic illustration of the delamination of the film.

A driving force for delamination occurs when the compressive stress within the film, $-\sigma_0$, of the film is larger than this value.

In the case of anodization of aluminum, the convertion of aluminum into alumina is accompanied by a large volume change; volume expand about 1.5 times. Therefore, a large compressive stress exists in the formed alumina film. The bond between alumina and aluminum is much stronger than the bond between alumina and silicon. When the alumina front reaches to the Si surface, the delaminate occurs and film buckles. But the surrounding of the newly formed voids is still aluminum, which has stronger bond with Si. When such remaining aluminum is anodized into alumina, the voids serve as stress releasing sites, which keeps this small area of alumina on the Si surface.

Considering the whole anodization process time, only a couple hundreds of seconds, we believe that stress-induced localized delimination is the formation mechanism of suce voids.

Effect of pore widening time on porous structure

The main advantage of porous aluminum oxide as a template is the tunability of the diameter of pores. The pore diameter can be tuned after anodization process The anodized alumina templates are dipped in phosphoric acid with different dipping time. The results are shown in Figure 5.10.

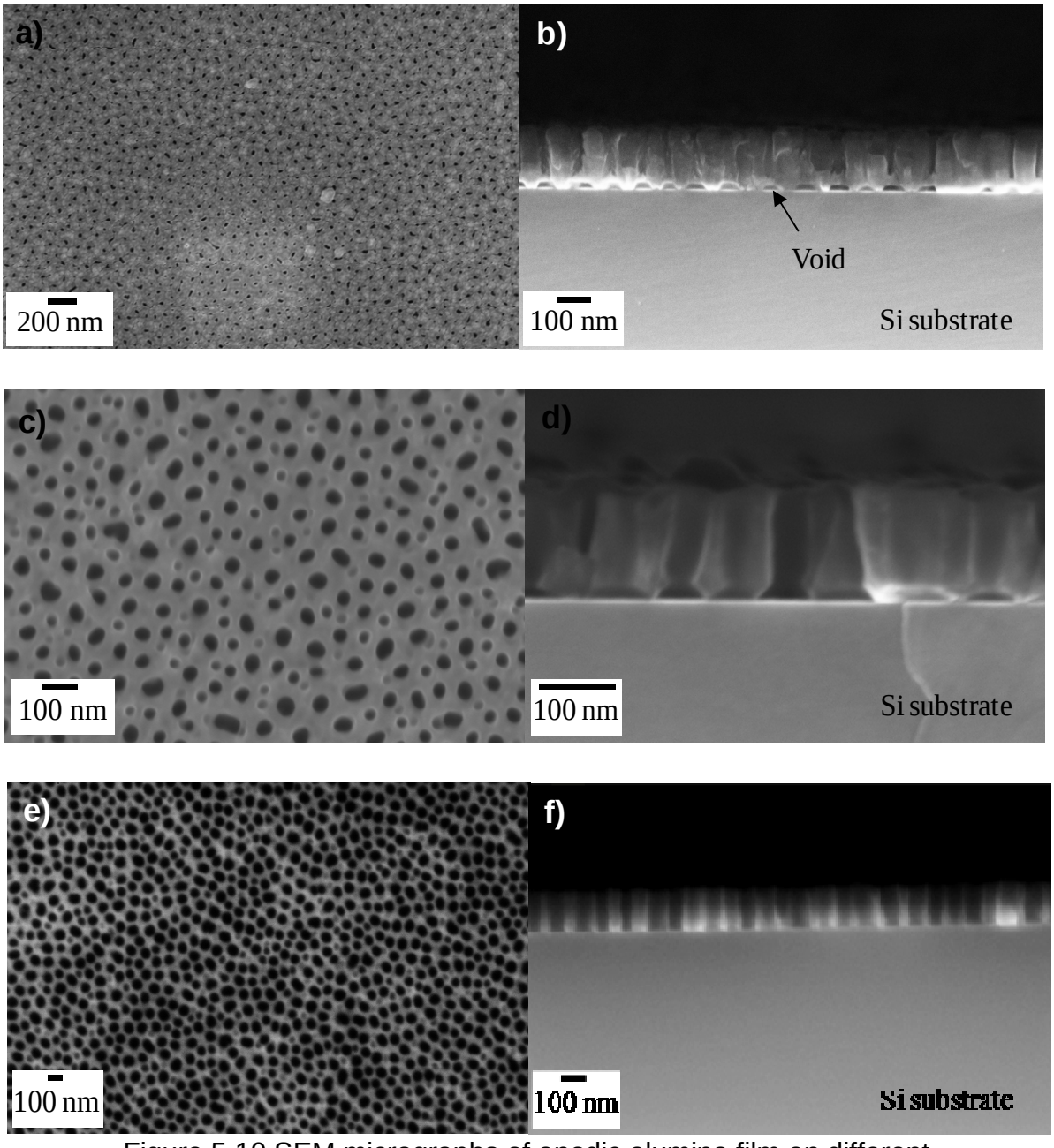

Figure 5.10 SEM micrographs of anodic alumina film on different pore widening time 0 (a,b), 20 (c,d), 40 (e,f) min

After anodization, AAO has small pores with voids underneath the barrier layer. Pores can be enlarged by simply immersing the sample into phosphoric acid. For a 20 min enlarging, the the barrier layer is partially etched, and the pore become connected to the voids, as shown in Figure 5.11. Generally, oxide layer of barrier layer is thinner than the oxide layer of pore wall. The porous structure has a

protrusion at pore wall because phosphoric acid partially etches both barrier layer and side wall. The diameter of porous alumina is increased from 40 nm to 60 nm. If pore-widening process is carried out in phosphoric acid for 40 min, the diameter of pores increased to 80 nm and the protrusion area is no longer visible, having a straight wall. The profile of this porous alumina template is that the pores are very straight through-holes, which is desirable for using as a mask for evaporation. Considering a 4-inch wafer with 100 nm patterns and a coverage of 50% can generate 500 billion (5×10^{11}) particles. This is comparable to the concertration of commercially available 100 nm collidal gold suspensions, which has 5×10^{9} nanoparticles per milliliter. The nanoparticles released from a 4-inch anodized wafer is able to reach a 100 ml suspension.

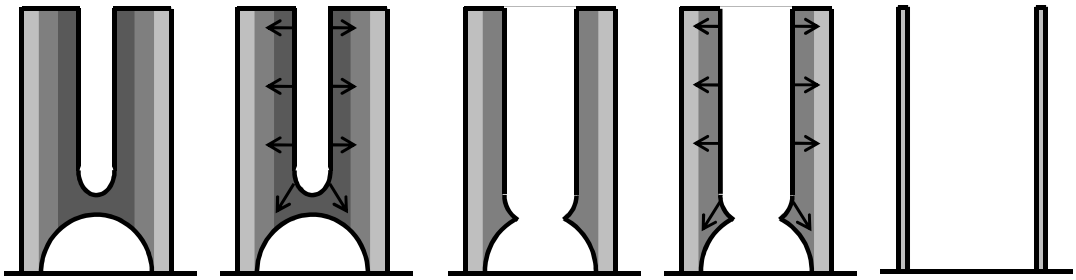

Figure 5.11 Schematic drawing of pore enlargement during immersing in acid.

The dissolution rate of the alumina changes with the location; different area has different dissolution rate. The rate increases from the pores wall (the hydrated aluminum hydroxide – the darker gray area) to the inside (the amorphous aluminum oxide – the lighter gray area). The alumina pores are initially filled with acid. The dissolution rate is faster at the beginning, then slows down when the inside alumina exposed. Since the voids are formed through different mechanism (delamination),

the voids wall consists of alumina with slower dissolution rate. This is the reason that a straight wall can be generated even with a protrusion (see Figure 5.11).

Effect of anodization time

The critical step to successfully generate ultrathin template is to stop the anodization process at the right time. The anodization process can be monitored by recording time-current transient (as shown in Figure 5.12). At the very beginning, current rapidly decrease due to the formation of insulating alumina layer. Then, current gradually increases because the barrier layer get etched and become thinner. When almost all metal become oxide, the current starts to drop.

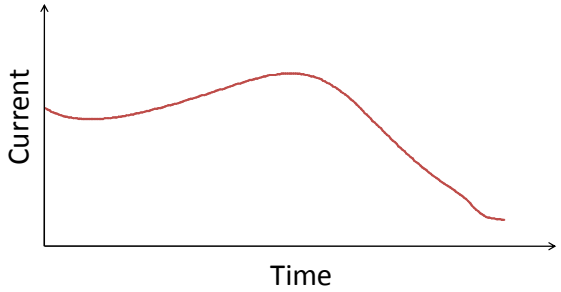

Figure 5.12 Anodization behavior of ultrathin porous alumina on Si substrate at 40V.

Figure 5.13 shows the result using templates with different anodization time. In this experiment, 150 nm aluminum is deposited on Si substrate. The anodization process is conducted at 40 V and the pore widening time is 40 min in 5% phosphoric acid. Then, metallic materials are deposited into pore of a mask. All parameters are kept in the same conditions, except anodization time.

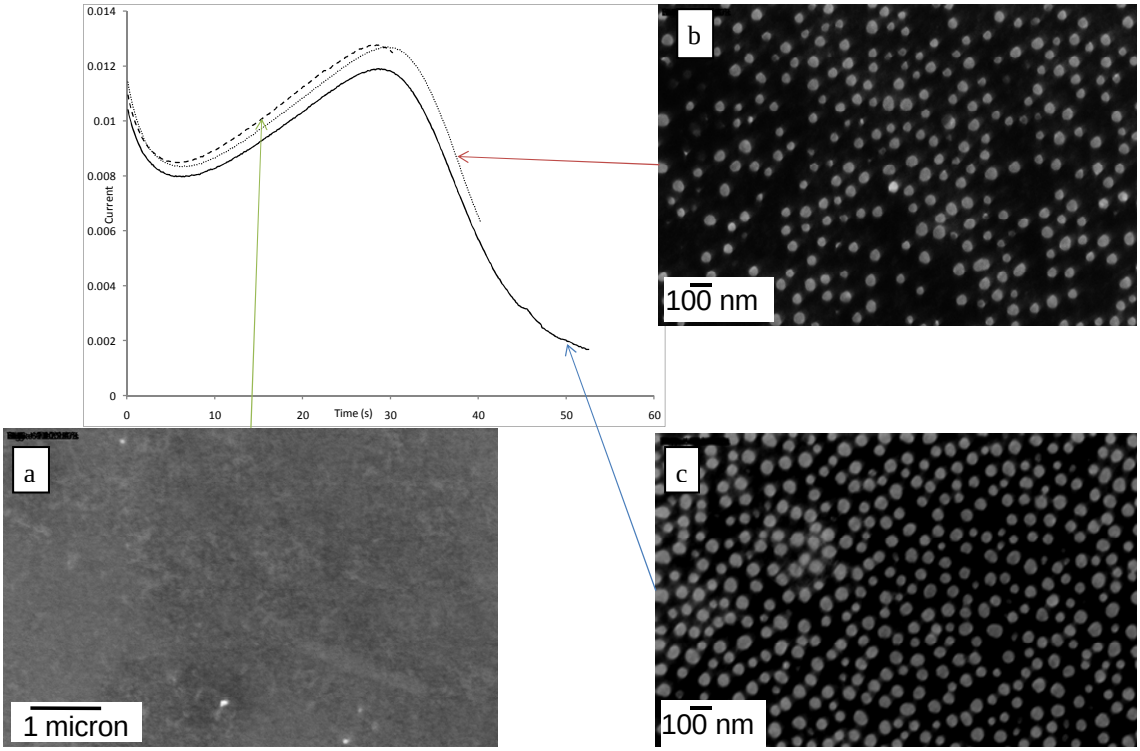

Figure 5.13 SEM micrographs of Cr/Au 30/50 Aº nanodisks produced with different anodization time of 150 nm Aluminum.

As shown in Figure 5.13, we stop the anodization process at 3 different anodization time; high, moderate, and low current (short, moderate, and long time). The current reaches to a stable plateau. Beyond this point, the continuation of the anodization will cause a sudden increase of current and oxide layer deliminate from Si substrate.

After anodization, each sample is dipped in 5% phosphoric acid for 40 min for pore enlargement. The metallic materials Cr/Au 30/50 Aº is evaporated into pores of a mask and then NaOH is used to remove the mask to expose nanoparticles on the Si substrate.

From the micrographs, it can be seen that If the anodization process stops when the current starts dropping, even after pore widening, there is no particles appear on Si substrate because pores do not reach to Si substrate. If anodization

process stops after the current drops but before the current reaches the minimum (moderate time), there are some disks on the substrate, indicating some pores reach to the surface. To produce large amount nanoparticles, the current should drop to the minimum point (long time). But any more anodization will cause the template peel off from the substrate after this point.

5.2.3. Fabrication of nanostructures by evaporation into ultra thin anodic alumina template

Truncated hollow nanocones using bottleneck AAO template

The hole template with protrusion (20 mins widening time) can actually be used as templates to produce new type of nanoparticles, truncated hollow nanocone, as shown in Figure 5.14.

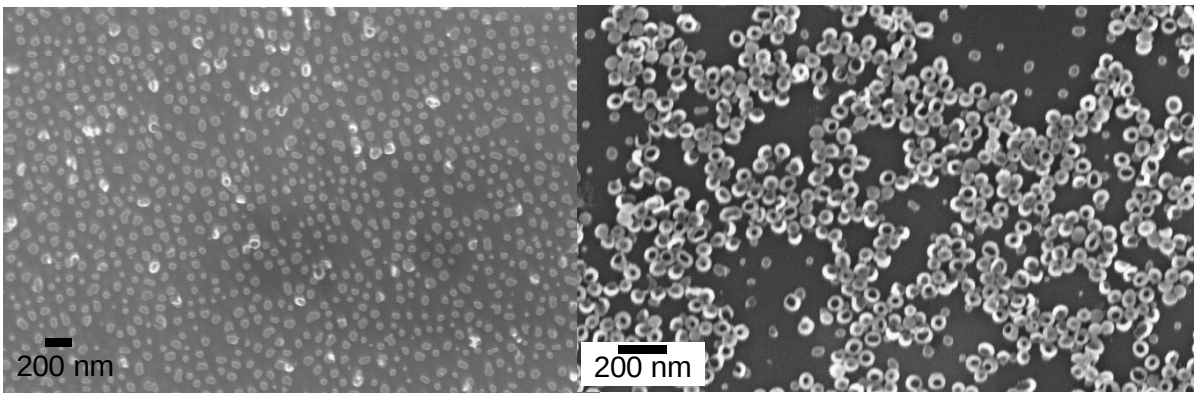

Figure 5.14 SEM micrographs of Cr 15 nm produced with different pore widening time, 20 (a) and 40 (b) min on 150 nm Aluminum.

15 nm Cr metal was evaporated into such template. Evaporated material deposited both on protrusion area and Si substrate. After dissolving the template, the deposit on protrusion area becomes truncated hollow nanocones (as shown in Figure 5.15). At the same time, the deposit on the substrate will become nanodisks. Therefore, such template can be used to simultaneously produce two nanostructures.

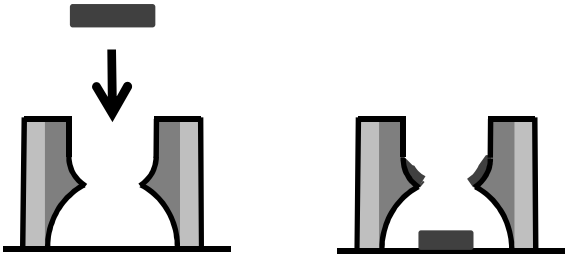

Figure 5.15 Schematic drawing of material deposition on bottleneck anodic alumina template.

Nanodisks using straight-pore AAO template

After anodization and pore widening process, the nanodisks can be produced by evaporation into ultra thin porous aluminum oxide template. First, we deposited Cr, as an example, into the ultrathin AAO template. The results are shown in the following micrographs.

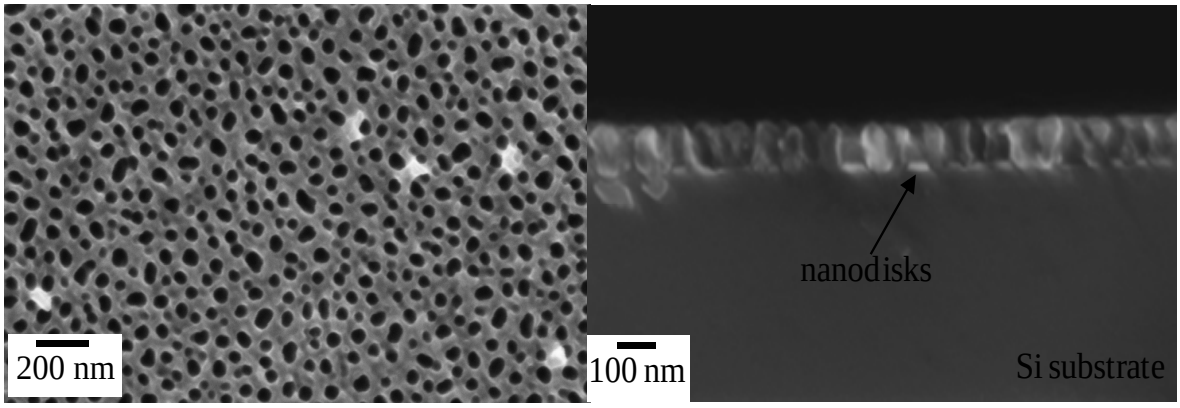

Figure 5.16 SEM micrographs of 70 nm nanodisks of Cr fabricated using evaporation on anodization before removing anodic alumina template.

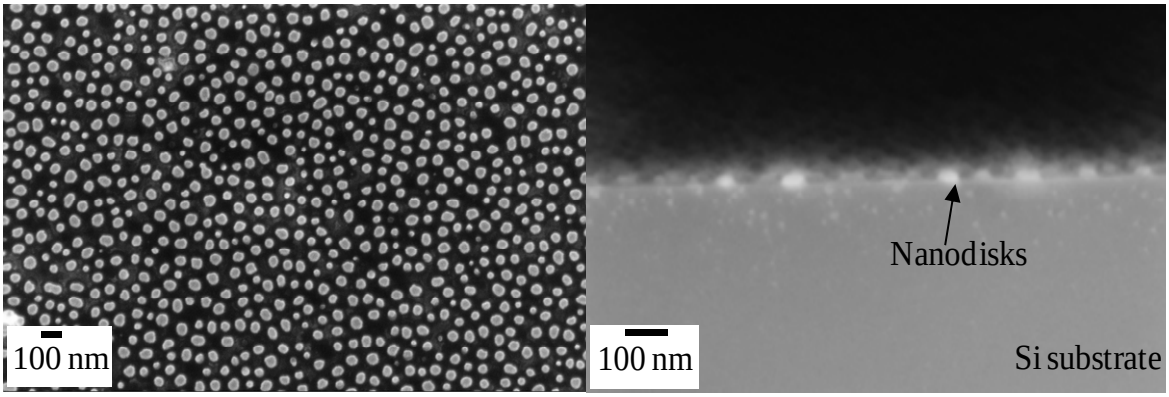

Figure 5.17 SEM micrographs of 70 nm nanodisks of Cr fabricated using evaporation on anodization after removing anodic alumina template.

The template used is the porous aluminum oxide template after 40 mins pore widening. Evaporation is a preferred deposition tool to deposit materials into small holes to form nanodisks because the deposition is highly direction so the side wall deposition is very small. Chromium atoms can easily pass through porous aluminum oxide and reached the surface of Si substrate. During the deposition, a low (4 μTorr) vapor pressure is used to maximize the directional deposition. The source heated from room temperature, the evaporation is conducted until the thickness of the metal reached 15 nm with an evaporation rate 0.6-1 nm s^{-1}. We chose chromium (Cr) metal as an example, because Cr has a good adhesion to Si substrate so the nanodisk surface is very smooth, as shown in Figure 5.16 and 5.17. Cr is also deposited on the top of the template. But porous aluminum oxide can easily be removed using chemical etching such as 1M NaOH for only several minutes, resulting in well-dispersed Cr disks on Si substrate, as shown in micrograph. The interpore distance between the nanodisks is about 40-70 nm, which is in good agreement with the interpore distance of porous aluminum oxide.

Si nanopillars using Cr hard mask

Porous aluminum oxide mask can be used as a part of process to produce nanopillars. In this case, 10 nm Cr is deposited into the template followed by the removal of the template using NaOH, which produces Cr nanodisks on Si substrate. Such nanodisks can be used as hard mask for reactive ion etching for Si. Using this process, we have fabricated sub-100 nm Si pillars, which is shown in Figure 5.18.

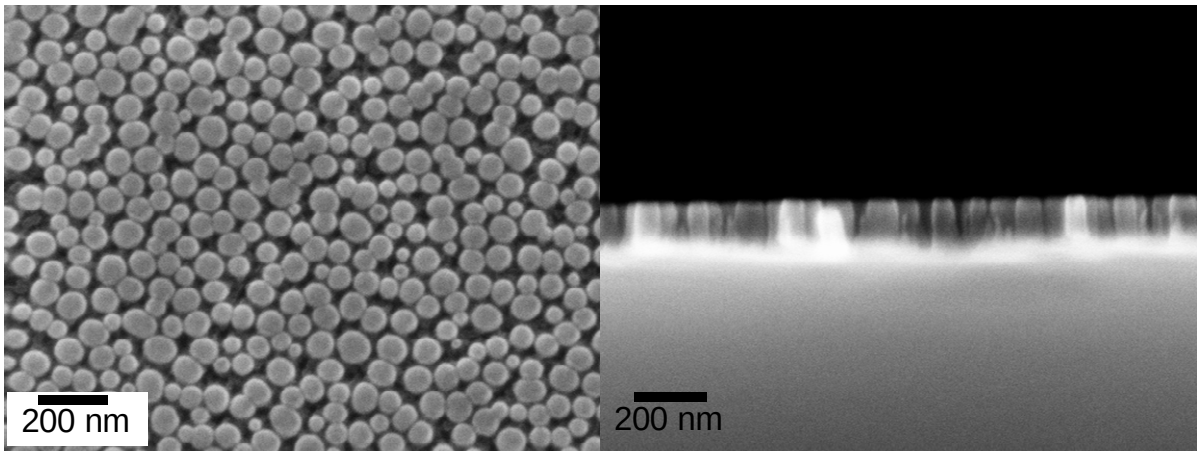

Figure 5.18 SEM micrographs of Si pllars produced by RIE on Cr mask

CHAPTER 6

FABRICATION OF DESIGNED MAGNETIC NANODISKS BY EVAPORATION INTO ULTRA THIN ANODIC ALUMINA TEMPLATES

6.1. Granular magnetic nanodisks

Porous aluminum oxide can be used as a mask to produce magnetic nanodisks. Magnetic nanodisks of Au(4 nm)/Fe(3 nm) and Au(4 nm)/Fe(1.5)/Au(4) /Fe(1.5) are deposited and characterized.

Magnetic properties of nanodisks are characterized using vibrating sample magnetometer (VSM) after dissolving porous membrane. The hysteresis loops are measured with the external field parallel to the disk planes. The results are shown in Figure 6.1 and 6.2.

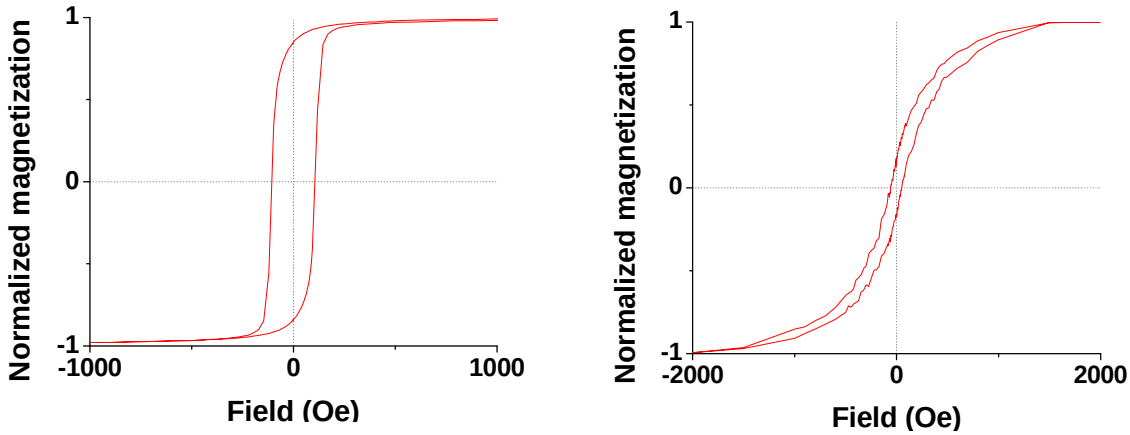

Figure 6.1 Magnetic characteristics of Au(4 nm)/Fe (3nm) using evaporation on ultra thin anodic; bulk film(left), particle after removal anodic alumina template(right).

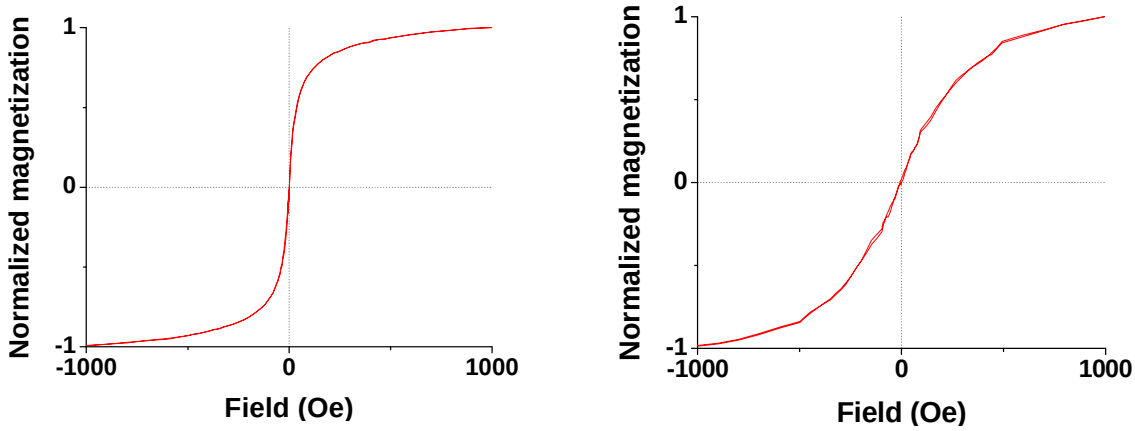

Figure 6.2 Magnetic characteristics of Au(4 nm)/Fe(1.5)/Au(4)/Fe(1.5) using evaporation on ultra thin anodic; bulk film(left), particle after removal anodic alumina template.

The hysteresis loop of 3 nm Fe bulk film clearly shows high remanent moment and coercivity. However, the hysteresis loop of 1.5 nm Fe thin bulk film shows no remanent moment and coercivity with a fairly low saturation field, indicating superparamagnetic state. Similarly, for the particle cases, the remanent moment and coercivity reduce to zero when thickness decreases from 3 nm to 1.5 nm. Reducing the film thickness to change the magnetic behavior from multidomain domain to superparamagnetic is the indication of that thinner film has not become continuous film, still separated islands.

6.2. Multilayered magnetic nanodisks

An effect of artificial domain wall thickness is studied. The interaction between two magnetic layers is dependent on the spacing layer thickness. Samples with the different spacing layer thickness are fabricated. The configurations of magnetic nanodisks are (Cr 3/Cu 12/Cr 5/NiFe 5/Cr 5/NiFe 5/Cr 5nm) and (Cr 3/Cu 12/Cr 5/NiFe 5/Cr 10/NiFe 5/Cr 5nm). Copper is used to be a sacrificial layer to release nanoparticles into solution. The results are shown in Figure 6.3 and 6.4.

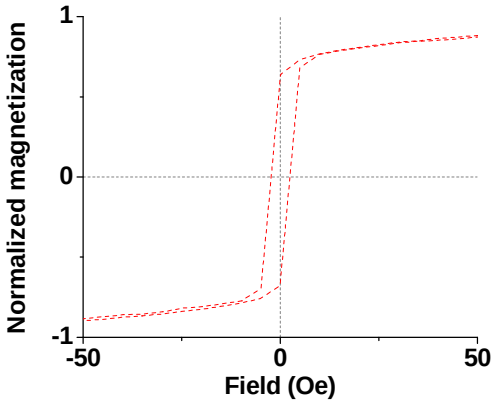

Figure 6.3 Magnetic characteristics of bulk film
(Cr 3/Cu 12/Cr 5/NiFe 5/Cr 5/NiFe 5/Cr 5nm)
using evaporation on Si substrate.

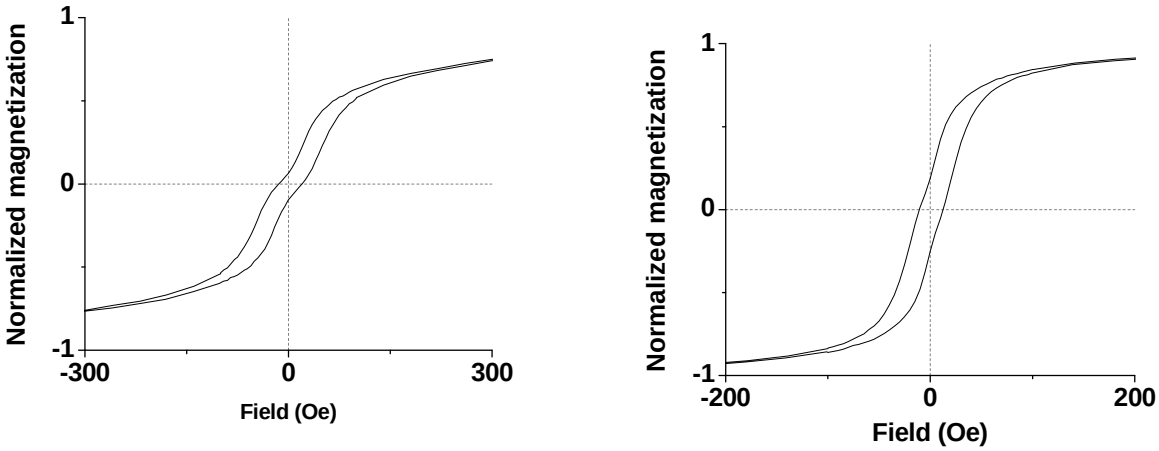

Figure 6.4 Magnetic characteristics of nanodisk (left)
(Cr 3/Cu 12/Cr 5/NiFe 5/Cr 5/NiFe 5/Cr 5nm) and
(right) (Cr 3/Cu 12/Cr 5/NiFe 5/Cr 10/NiFe 5/Cr 5nm)
using evaporation.

The hysteresis loop of typical bulk film of the sample with 5 nm spacing layer shows a high remanence, indicating the there is no interaction between two magnetic layers in bulk film. The multilayer hysteresis loop from thin non magnetic spacing layer has low remanence and high saturation field, which is expected according to our design. This is because the magnetostatic interaction is stronger than the thick non magnetic spacing layer case.

Unlike the sharp change shown in our expected hysteresis loops, the measured hysteresis loops show a gradual change of the magnetic moment. This is the result of the saturation field distribution (SFD) of nanodisks. This saturation field distribution include the switching field distribution for single layers and the distribution of interaction fields between these two layers. For the distribution of interaction fields, there are two main contributors, namely, the variation of magnetostatic interaction between the two layers, and the variation of exchange coupling through the spacing layer. The magnetostatic interaction depends on the magnetization structure in each layer. Exchange coupling is more sensitive to pinholes in the spacing layer, the thickness variations and the intermixing of the layers at the edges of the nanodisks. More controlled experiments are needed to determine the role of these two contributors in the distribution of the interaction field.

To fully characterize the magnetic properties for an assembly of multilayered nanodisks, switching field and interaction field distributions and the correlation between them are needed. We uses a simplified model by assuming that the interaction fields are constant and attributing the gradual change of the magnetic moment in hysteresis loops solely to the switching field distribution of the single layers.

The value of interaction field can be taken as the shift of the upper part of the loop relative to the zero applied field, which is about 34 Oe. The average switching field for single layer is the half width of the upper (or lower) part of the loop, which is about 12 Oe. We assume that the switching field distributions of the NiFe and Co layer follow a log normal distribution, a computer simulation is performed to simulate

the hysteresis loop. The Matlab code is shown below and the result is shown in Figure 6.5. The fitting parameter is the standard deviation of the switching field.

```
Total_number_of_particles =1000;
M = 1 * Total_number_of_particles; % total moment
M_LayerOne = 0.50; % LayerOne Moment
M_LayerTwo = 1 - M_LayerOne; % LayerTwo Moment
Mean_Hsw_LayerTwo = 12;
Mean_Hsw_LayerOne = 12;
Std_LayerOne = 30;
Std_LayerTwo = 30;
z1 = randn(Total_number_of_particles,1);
Z2 = randn(Total_number_of_particles,1);
H_LayerTwo_to_LayerOne = 34;
H_LayerOne_to_LayerTwo = 34;
Moment = zeros(31,1);
Field = zeros(31,1);
Hsw_LayerTwo = abs(Mean_Hsw_LayerTwo + Std_LayerTwo * Z2);
Hsw_LayerOne = abs(Mean_Hsw_LayerOne + Std_LayerOne * Z1);
Direction_of_LayerTwo = ones(Total_number_of_particles, 1);
Direction_of_LayerOne = ones(Total_number_of_particles, 1);
n=0;
for Ha = 300 : -10 : -300
 for i = 1:Total_number_of_particles
   % For LayerOne layer
```

```
  % First check if it is in the same direction of Ha
  if ((Ha - Direction_of_LayerTwo(i) *
H_LayerTwo_to_LayerOne)/Direction_of_LayerOne(i) < 0) &((Ha -
Direction_of_LayerTwo(i) * H_LayerTwo_to_LayerOne) <= -
Hsw_LayerOne(i))
        M = M - 2*M_LayerOne;
        Direction_of_LayerOne(i) = -1 * Direction_of_LayerOne(i);
  end
  % For LayerTwo layer
  if ((Ha - Direction_of_LayerOne(i) *
H_LayerOne_to_LayerTwo)/Direction_of_LayerTwo(i) < 0) &((Ha -
Direction_of_LayerOne(i) * H_LayerOne_to_LayerTwo) <= -
Hsw_LayerTwo(i))
        M = M - 2*M_LayerTwo;
        Direction_of_LayerTwo(i) = -1 * Direction_of_LayerTwo(i);
  end
 end
 n=n+1;
 Moment(n) = M/Total_number_of_particles;
 Field(n) = Ha;
end
for Ha = -300 : 10 : 300
 for i = 1:Total_number_of_particles
  % For LayerOne layer
```

```
   % First check if it is in the same direction of Ha
   if ((Ha - Direction_of_LayerTwo(i) *
H_LayerTwo_to_LayerOne)/Direction_of_LayerOne(i) < 0) &((Ha -
Direction_of_LayerTwo(i) * H_LayerTwo_to_LayerOne) >= Hsw_LayerOne(i))
            M = M + 2*M_LayerOne;
            Direction_of_LayerOne(i) = -1 * Direction_of_LayerOne(i);
   end
      % For LayerTwo layer
   if ((Ha - Direction_of_LayerOne(i) *
H_LayerOne_to_LayerTwo)/Direction_of_LayerTwo(i) < 0) &((Ha -
Direction_of_LayerOne(i) * H_LayerOne_to_LayerTwo) >= Hsw_LayerTwo(i))
            M = M + 2*M_LayerTwo;
            Direction_of_LayerTwo(i) = -1 * Direction_of_LayerTwo(i);
   end
 end
 n=n+1;
 Moment(n) = M/Total_number_of_particles;
 Field(n) = Ha;
end
hold on
plot(Field, Moment,'-k')
```

The hysteresis loop is shown as Figure 6.5.

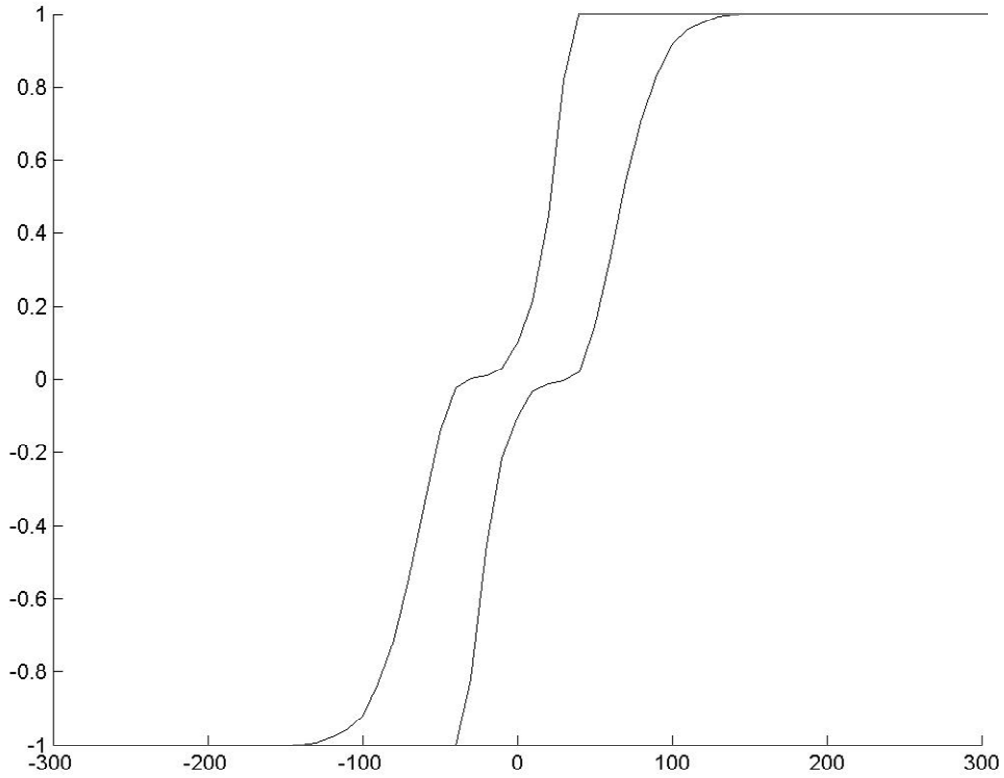

Figure 6.5 The hysteresis loop of a simplified model

The simulated result is in a good agreement with the low-field part of the measured hysteresis loop. But the high-filed part cannot be fit in this simple model. This indicates that there exist other nanodisks which have much large switching field. Those can be nanodisks with porous spacing layers, where two layers are not magnetically separated, and they behave just like single domain particles with very high switching fields.

CHAPTER 7

FABRICATION OF DESIGNED NANODISKS BY ELECTRODEPOSITION INTO THICK ALUMINUM OXIDE TEMPLATES

We have demonstrated that using evaporation and ultra thin AAO templates designed nanodisks can be fabricated and these nanodisks possess designed magnetic properties. However, the evaporation process involves vacuum, which may be too expensive to produce large amounts of nanoparticles. To reduce the fabrication cost, we explored using electrodeposition to generate nanodisks. In this chapter, the conditions and experimental results of fabrication of multilayers Au magnetic nanodisks are described.

For electrodeposition, very thick AAO membrane can be used, and many multilayered nanodisks can be produced in one pore (channel) of alumina template, as shown in Figure 7.1.

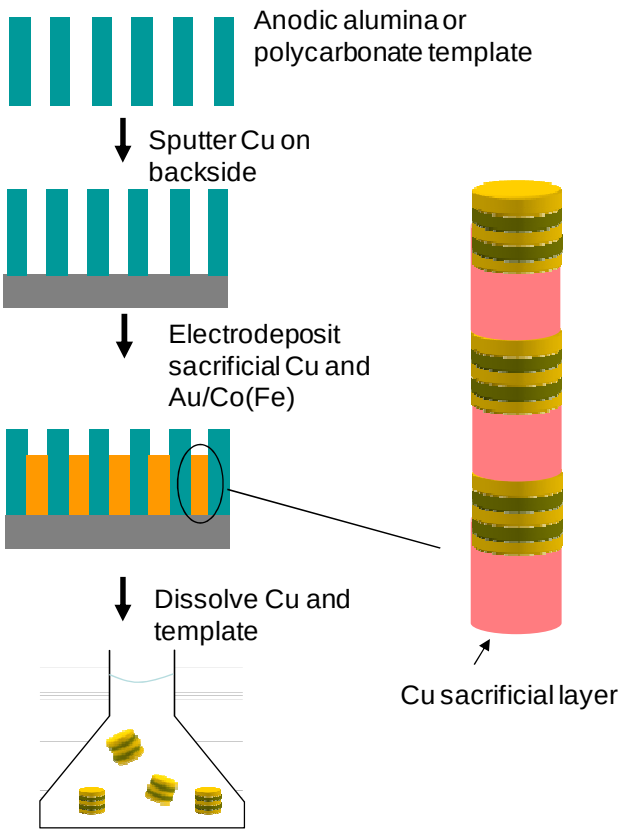

Figure 7.1 Illustration of the process of using anodic alumina membrane to fabricate designed nanoparticles using Au/Co(Fe) one bath electrodeposition.

7.1. Layer-by-layer electrodeposition

The multilayered magnetic nanorods can easily be fabricated by electrodeposition of each layer into templated (as shown in Figure 7.2). However, since after each layer deposition, electrolyte has to be changed, this process is very time-consuming. More importantly, the interfaces between layers are not sharp.

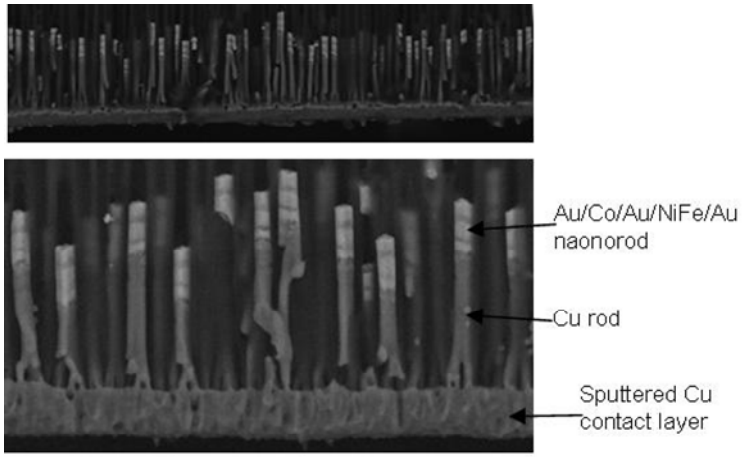

Figure 7.2 SEM micrograph of multilayer magnetic nanorods electrodeposited inside anodic alumina template.

To solve these problems, we developed a process to deposit Au and Fe or Co from one-bath electrolyte.

7.2. Deposition of multilayers of Au-Co from one electrolyte bath

Electrolyte for Au-Co multilayers

Since Au and magnetic metals (Co, Fe, Ni) have very different reduction potential, It is possible to mix Au complex ions with these metal ions in one electrolyte, and just changing the deposition potential to selectively deposition different materials.

The electrolyte used for the deposition of Au and Co consists of cobalt sulfate hepta hydrate ($CoSO_4.7H_2O$) potassium gold cyanide ($KAu(CN)_2$). Potassium hydroxide (KOH) is utilized to adjust pH of the electrolyte. The electrodeposition was conducted at room temperature. Following table presents the conditions for the preparation of electrolyte.

Table 7.1 Chemical composition of the electrolyte used in Au/Co deposition.

Chemical used	Molecular Formula	Composition
Cobalt Sulfate Hepta Hydrate	$CoSO_4.7H_2O$	0.285M
Citric Acid	$C_6H_8O_7$	0.8M
Potassium Gold Cyanide	K $Au(CN)_2$	$3X10^{-4}$M

The concentration of gold complex ions is only about $3X10^{-4}$M while the concentration of cobalt ion is 0.285M. This huge concentration difference is necessary. The reduction potential in aqueous solution at 25°C for gold (+1.50V) is much more positive than the reduction potential of cobalt (-0.28V). Au can be deposited without any Co deposition if the potential is negative than Au deposition potential but positive than Co deposition potential. However, when Co is deposited, Au can also be deposited, which will deposit Au-Co alloy instead of pure Co. However, the concentration of gold is very small compared to the concentration of cobalt; the amount of gold deposition at high potential is very low. Therefore, gold and cobalt alloy formation is negligible.

Cyclic voltamograph for this electrolyte is shown in Figure 7.3. Cyclic voltammetry is scanning from -0.1V to -1.25V to find the right voltages for gold and cobalt deposition. It shows that the deposition of gold reach the maximum around -0.49V while deposition of Cobalt need to be carried out at potential more negative than -1V.

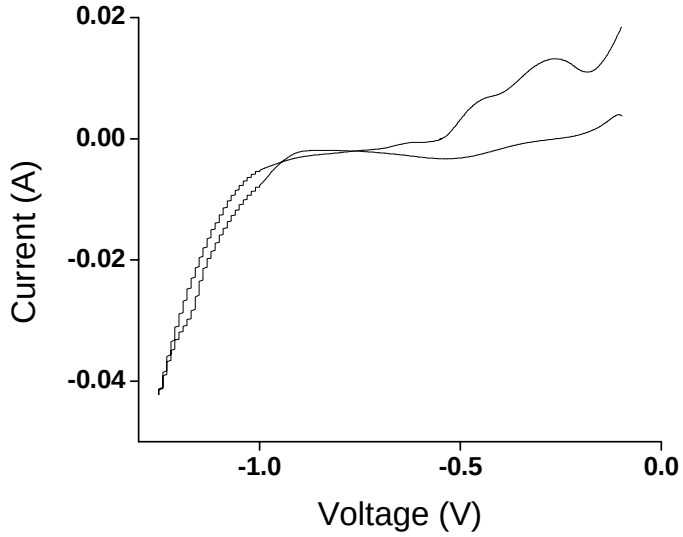

Figure 7.3 Cyclic Voltammetry of Au-Co one-bath electrolyte.

The fabrication of Au-Co multilayers from this single electrolyte bath is affected by several parameters such as concentration and applied potential. The Co film deposition can be characterized by measuring magnetic properties of the film. The effect of pH, concentration of gold, and applied potential on cobalt are studied. For comparison, all samples are cut into the same area and measured using VSM. In all experiments, the substrate is a gold coated on silicon wafer.

Effect of pH on Co film formation

The pH of electrolyte plays an important role in electrodeposition. An effect of pH is studied to obtain the right condition for cobalt deposition. All the parameters of experiments are kept in the same condition; expect the pH of the electrolyte. The results are shown in Figure 7.4 and Table 7.2.

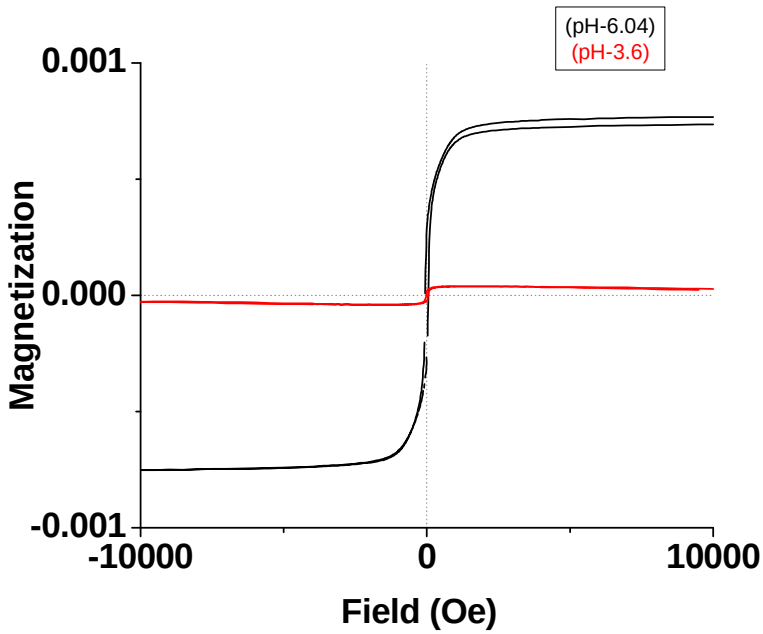

Figure 7.4 Variation in pH

Table 7.2 Variation of magnetic moment, remanence and coercivity with pH

pH	Co con.	Au Con.	Time	Moment	Remanence	Coercivity
3.61	0.285M	$3X10^{-4}$ M	1000 sec	$4X10^{-5}$ emu	$1.88X10^{-5}$ emu	30.2 Oe
6.04	0.285M	$3X10^{-4}$ M	1000 sec	$8X10^{-4}$ emu	$2.87X10^{-4}$ emu	60.1 Oe

The magnetic moment of the sample deposited from an electrolyte with pH 6.04 is $4X10^{-5}$ emu and the moment decreases more than 10 times if the pH goes down to 3.5. As pH increases, cobalt deposition and magnetic moment also increase. However, gold deposition dramatically decreases as the pH of electrolyte increases. Therefore, pH has to be maintained at pH 3.5 to 4 for multilayer deposition.

Effect of gold Concentration on Co film formation

The concentration of gold ion also affects the deposition of Co. The magnetic moment increases sharply if the concentration of gold is increased beyond $3X10^{-4}M$, as shown in Figure 7.5.

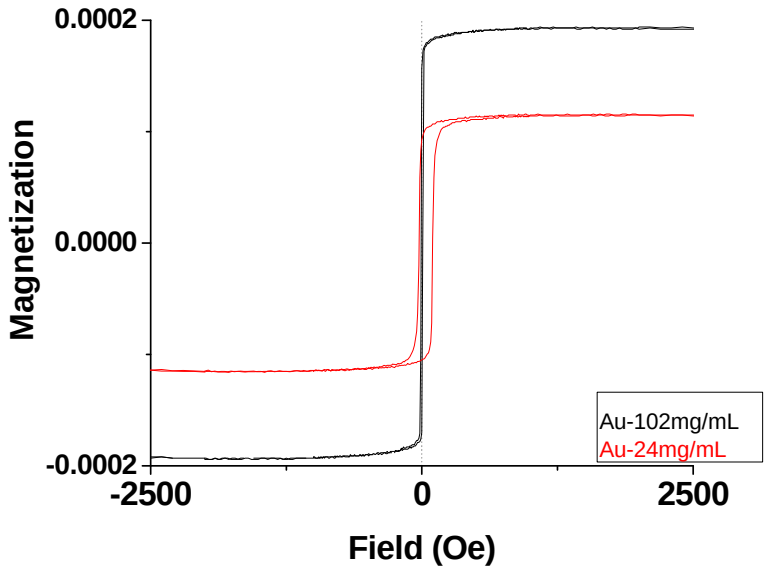

Figure 7.5 Variation in Gold Concentration

The results from the above hysteresis loop can be summarized in the table below:

Table 7.3 Variation of magnetic moment, remanence and coercivity with Au concentration

pH	Co Con.	Au Con.	Time	Moment	Remanence	Coercivity
3.65	0.285M	$5.17X10^{-3}M$	200 sec	$1.2x10^{-4}$emu	$1.57X10^{-4}$ emu	28.31 Oe
3.65	0.285M	$3X10^{-4}M$	200 sec	$2x10^{-4}$ emu	$9.32X10^{-5}$ emu	14.99 Oe

The fact that increasing the gold concentration the magnetic moment also increases is actually desired. However, there is a limitation because cobalt is deposited at a potential of -1V and gold at -0.49V. During cobalt deposition, small

amount of gold is also deposited which leads to the formation of gold-cobalt alloy. This gold-cobalt alloy is highly undesirable. The chance to form gold-cobalt alloy becomes high when the concentration of gold is beyond $3X10^{-4}$M. Therefore, the concentration of gold and the desired magnetic moment has to be balanced.

Fabrication process of Au-Co multilayered nanorods

Multilayer bulk film sample of gold and cobalt is fabricated using above-mentioned single bath Au/Co electrolyte with cobalt deposited at -1V and gold deposition at -0.49V. The sample consists of 5 alternating Au/Co layers with 1000 seconds deposition for each Au layer and 30 seconds deposition for each Co layer. The result is shown in Figure 7.6**.**

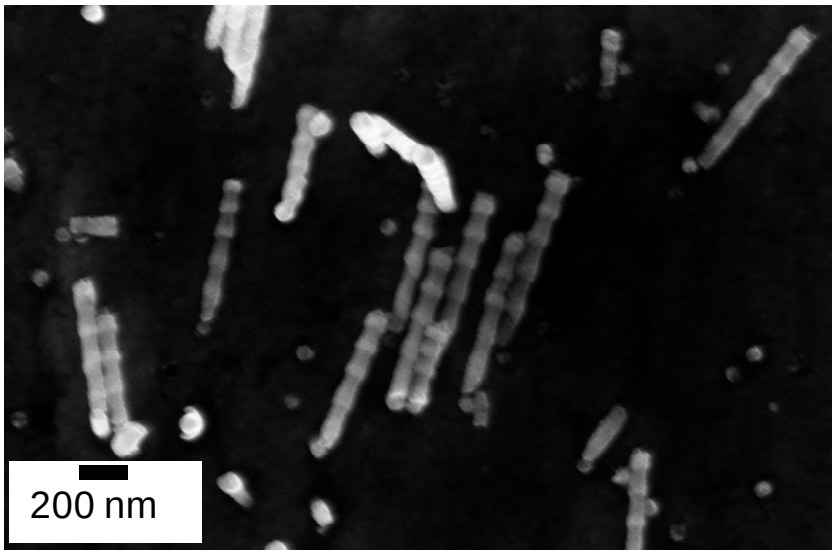

Figure 7.6 SEM micrograph of a sample (Au 1000s/Co 30s)$_5$.

Multilayered structures are also deposited in polycarbonate membrane, which is similar to AAO templates with 100 nm channels.From micrograph, gold and cobalt multilayer nanowires having different contrast are clearly shown. The different contrast in nanowires from the micrograph indicates two materials. Gold is brighter than cobalt because gold has atomic number higher than cobalt.

7.3. Deposition of multilayers of Au-Fe from one electrolyte bath

We have also developed a process to deposit Au and Fe from single bath electrolyte. Fe is considered as biocompatible material. For in vivo applications, Co must be replaced with Fe.

Electrolyte for Au-Fe multilayers

The electrolyte used for the deposition of Au and Fe consists of iron sulfate ($FeSO_4$) and potassium gold cyanide ($KAu(CN)_2$). Potassium hydroxide (KOH) is utilized to adjust pH of the electrolyte. The electrodeposition was conducted at room temperature. Following table presents the conditions for the preparation of electrolyte.

Table 7.4 Chemical composition of the electrolyte used in Au/Fe deposition.

Chemical	Concentration
$FeSO_4$	0.29 M
Citric acid	0.49 M
$K\ Au(CN)_2$	1 mM
KOH	1.07 M

The concentration of gold complex ions is only about 1mM while the concentration of iron ion is 0.29M. Au can be deposited without any Fe deposition. However, when Fe is deposited, Au can also be deposited, which will deposit Au-Fe alloy instead of pure Fe. However, the concentration of gold is very small compared to the concentration of iron; the amount of gold deposition at high potential is very low. Therefore, gold and iron alloy formation is negligible.

Cyclic voltamograph for this electrolyte is shown in Figure 7.7. Cyclic voltammetry is scanning from -0.1V to -1.25V to find the right voltages for gold and iron deposition.

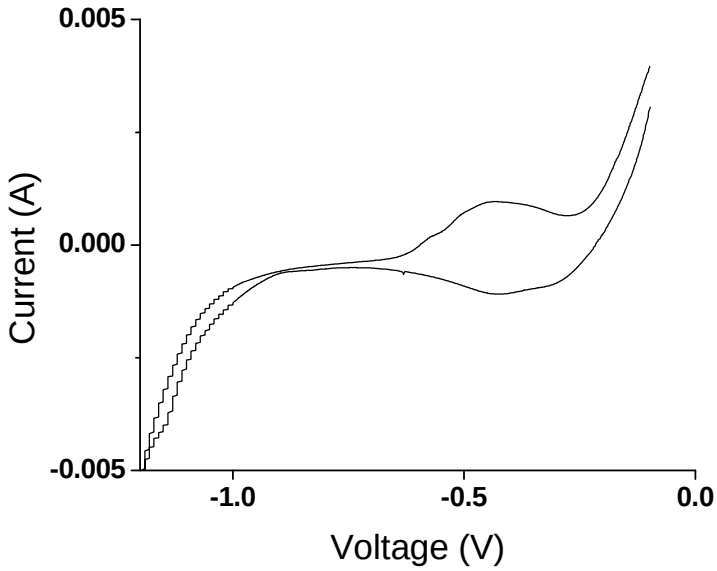

Figure 7.7 Cyclic Voltammetry of Au-Fe solution for potentials of Au and Fe.

The result shows that the deposition of gold reaches the maximum voltage around -0.45V. The deposition of iron need to be carried out at potential more negative than -1V.

Fabrication multilayered Au-Fe nanodisks

Electrodeposition is carried out using constant current. AAO membrane is used as the template. Copper is first deposited as the sacrificial layer for releasing the multilayered particles. Copper is deposited at -0.05V for 2 hours using copper sulfate electrolyte with pH3.5. 3 alternating Au/Fe layers are then deposited with 400 seconds Au deposition at -0.45V and 25 seconds Fe deposition at -1V. The final capping Au layer is deposited for 400 seconds. After deposition, the template is removed by NaOH. The SEM micrographs and magnetic property by VSM are shown in Figure 7.8.

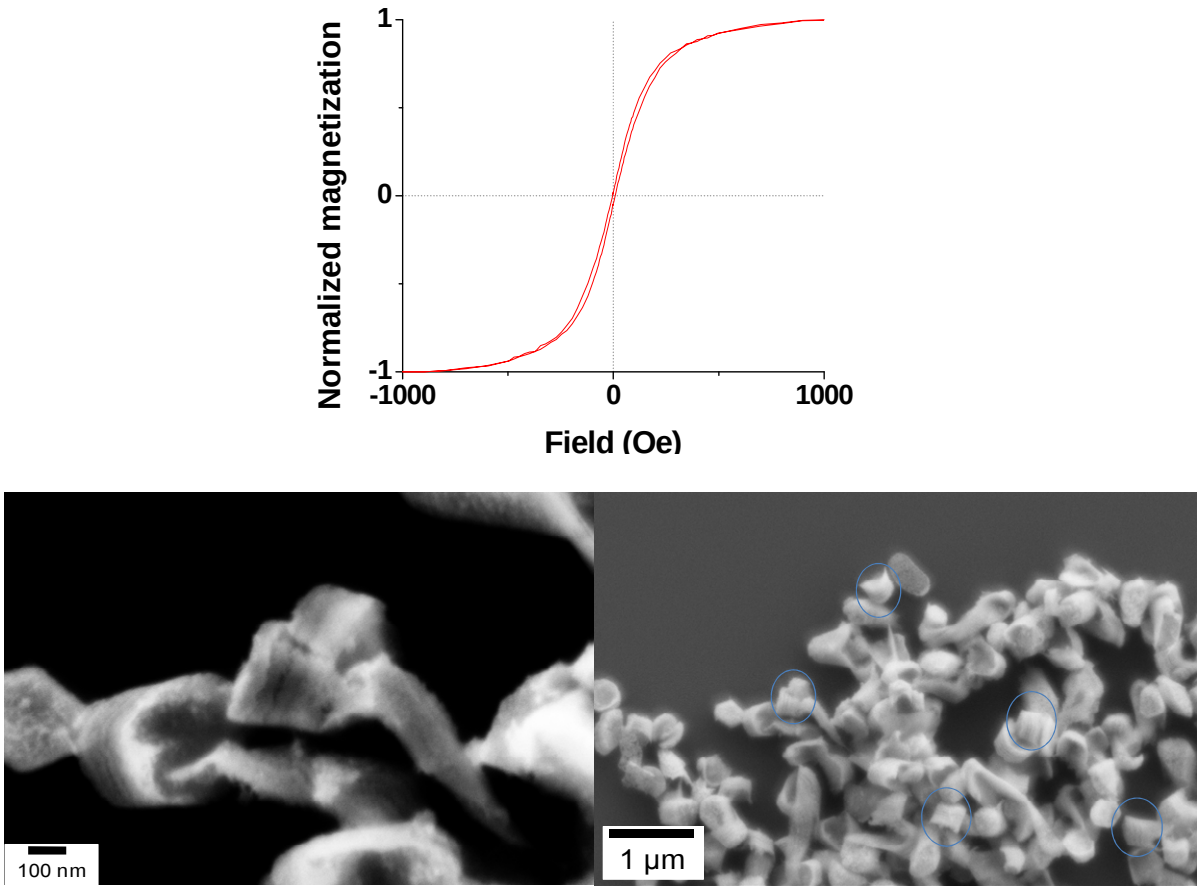

Figure 7.8 Magnetic characteristics and SEM micrograph
of Au/Fe nanodisk with copper as a sacrificial layer.

The remanence and coercivity of the sample is near zero, this indicates that the particles are superparamagnetic. In SEM micrograph, the bright area is gold, while the dark area is iron. The thickness of iron is about 5 nm. The superparamagnetic nature of particles suggests that at this thickness, granular structure still formed in gold matrix. At evaporated samples, granular structure form at the thickness less than 2 nm. This is reasonable since electrodeposition rate is much higher than evaporation rate; island growth is favored.

CHAPTER 8

FABRICATION OF DESIGNED NANODISK USING PILLAR BASED TEMPLATE

8.1. Fabrication of pillar-based template

AAO membranes having uniform and well separated pores of diameters 55 nm and a thickness of 60 µm (from Synkera Technologies, Inc.) have been utilized. Ag 500 nm is deposited using sputtering on one side (smooth side) of the membrane to block the pores and served as working electrode for electrodeposition. Then, gold is electrodeposited into pores to form gold rods with a length of about 5 µm. After deposition, the Ag layer is dissolved using nitric acid, and bottom surface of Au rods is exposed. A chemical-mechanical polish process is used to make the side of the membrane with Au deposition to be a flat surface. The solution for chemical-mechanical polish process is Au etchant (from Transene Company) mixed to regular metallographic diamond polishing solution. The alumina membrane on the polished surface is partially etched using sodium hydroxide to expose Au pillars. 50-nm of Cu sacrificial layer is evaporated onto pillars. The diameter of pillars is about 55 nm and every pillar is well separated, as shown in Figure 8.1. These sacrificial Cu pillars tip can be employed to fabricate magnetic nanodisks because of its smooth and flat surface.

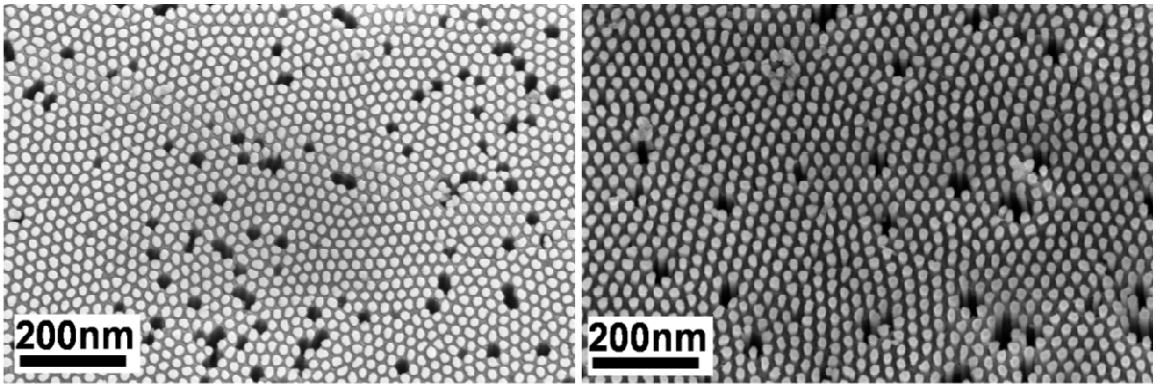

Figure 8.1 SEM micrographs of magnification view of 55nm Cu pillars

8.2. Fabrication of magnetic nanodisks using pillar-based template

The fabrication process using pillar template is shown in Figure 8.2. To fabricate multilayered magnetic nanodisks, the configuration of Au(10 nm)/Co(10)/Au(10)/NiFe(18)/Au(10) are deposited using sputtering where coated on top of Cu pillars tip, as shown in Figure 8.3. During the deposition, a low (2.5 mTorr) Ar pressure is used to maximize the directional deposition. In order to remove nanodisks from pillars tip, Cu etchant with Ni/Fe compatible is selected to dissolve Cu. SEM micrographs of nanodisks fabricated using this process are shown in Figure 8.3. The diameter of nanodisks is about 70 nm, which is larger than pillars tip diameter due to the film deposition covering the sidewall of pillars and enlarging the top surface. To minimize the sidewall coverage of pillars, evaporation is selected as a fabrication tool. Also, distance between the evaporation source and substrate needs to be increased.

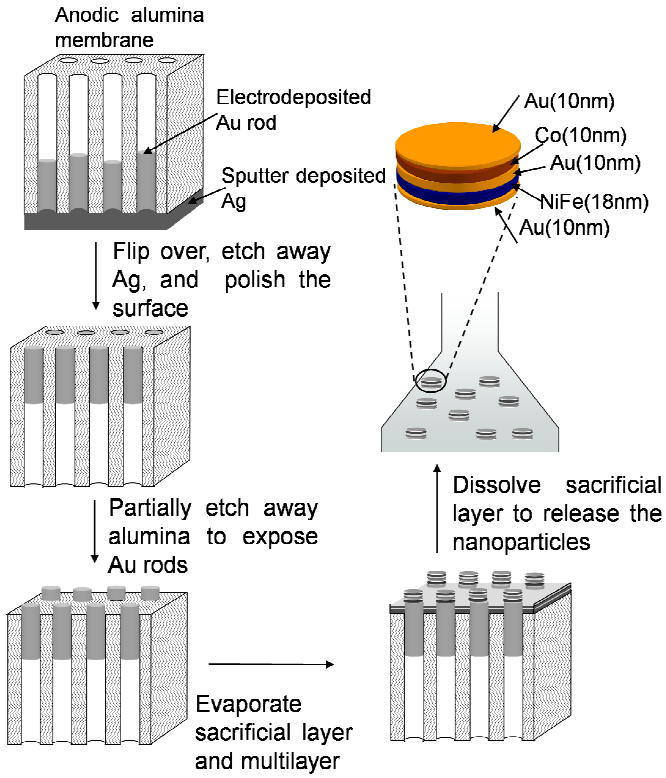

Figure 8.2 Illustration of the process of using anodic alumina membrane to form pillar template for generating nanoparticles.

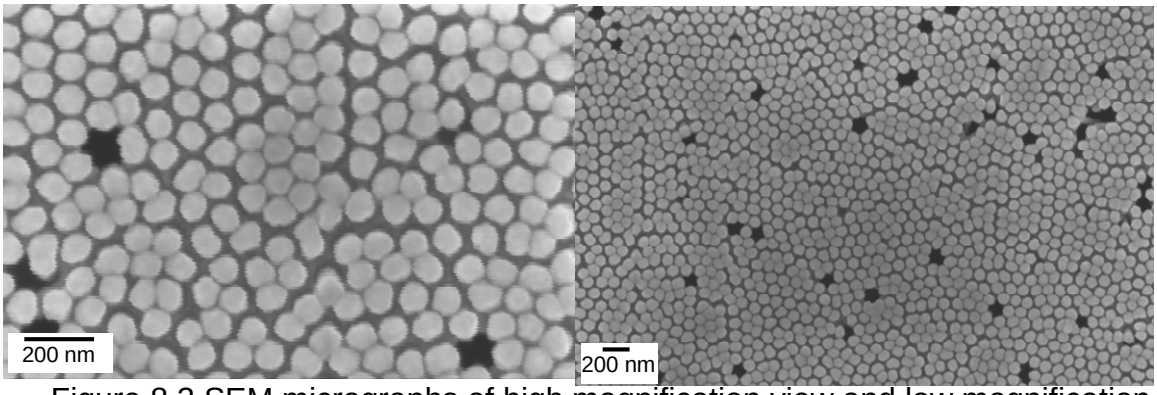

Figure 8.3 SEM micrographs of high magnification view and low magnification view of 70 nm nanodisks of (Au/NiFe/Au/Co/Au) fabricated using pillar-template-based synthesis.

8.3. Magnetic properties of magnetic nanodisks

Magnetic nanodisks are characterized using alternating gradient magnetometer (AGM) and measured before dissolving sacrificial layer. All hysteresis loops are measured with the external field parallel to the disk planes. The single

magnetic layer nanodisks with the same layer thickness as the double magnetic layer nanodisks, Au(10 nm)/Co(10)/Au(10)/NiFe(18)/Au(10), are characterized for comparison. The results are shown in Figure 8.4.

The hysteresis loop of multilayer for bulk film clearly shows two separate switching; one from soft layer and another from hard layer. The multilayer hysteresis loop from the experimental result is similar to the constructed hysteresis loop by adding two single magnetic layers together. This indicates that the interaction between two magnetic layers from bulk film is very small. Breaking the film into small nanodisks changes the magnetic behavior from multidomain to single domain, which is indicated by the increase of coercivity. Nanodisks from single magnetic layers still have relatively high remament moment. However, the remanence of nanodisks from multilayer decreases dramatically indicating a strong magnetostatic coupling between two magnetic layers in each nanodisk, which is demonstrated by comparing the measured hysteresis loop with combined hysteresis loop from two single magnetic layer. The very low remanence is due to the magnetic being deposited at the side wall and in between the pillars. The result shows that the multilayer magnetic nanodisks in single domain range can have low remanence, which is desirable for biomedical applications. The calculated magnetic moment of this configuration for each nanodisk is about 0.1 pico-emu, and the measured collective moment is about 6×10^{-5} emu for estimated 6.7×10^{8} disks. The value of measured moment for each nanodisk is close to the calculated value. The moment for each multilayer nanodisk is equivalent to the moment of co nanodisk with 100 nm of diameter and 10 nm of thickness.

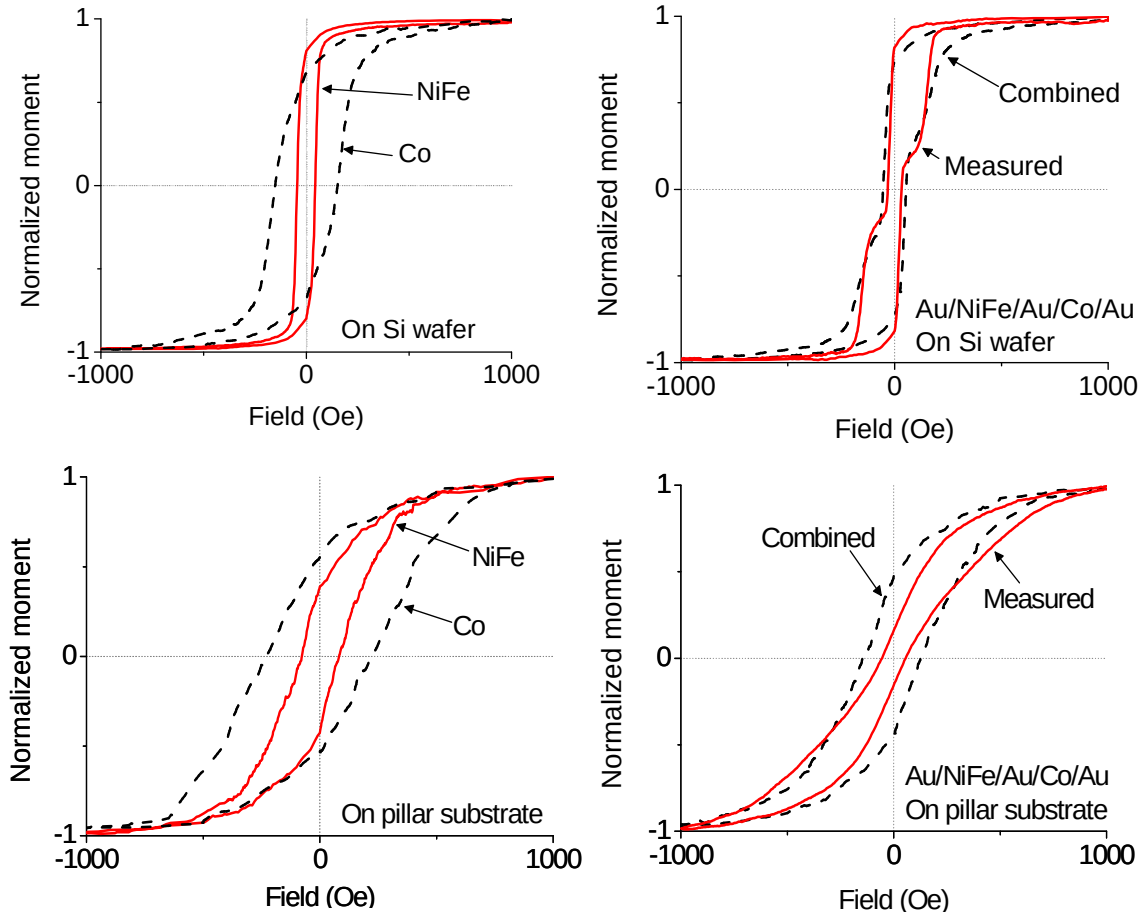

Figure 8.4 Hysteresis loops of single- and double magnetic layer flat thin film and nanodisks. Combined hysteresis loop is constructed by mechanically adding two single-layer loops together.

In pillar-template-based synthesis, the reusability of the template and scalability of the process make it affordable to fabricate nanodisks in solution. In last decade, several simple generation tools such as interference lithograhy, nanosphere lithography, anodic alumina, and imprint lithography have been developed to fabricate nanomagnets for data storage media [42, 45-47]. A well-ordered nanomagnet structure has to be obtained using these techniques. However, for the purpose as template for particle fabrication, ordering is not required. This further simplifies the pattern generation process, making it even more inexpensive.

CHAPTER 9

SUMMARY

We designed two new types of high moment magnetic nanoparticles for bioapplications; multilayer and granular nanodisks. In these nanoparticles, two important requirements for bioapplications, high magnetic moment and near-zero remanence, are achieved. Multilayered nanodisks consist of two magnetic layers separated by a non-magnetic layer with two capping layers. Magnetic properties are controlled by magnetostatic interlayer coupling between two magnetic layer. Capping layers such as gold provide functionalization sites for biomolecule attachment. For granular magnetic nanodisk, superparamagnetic nanoparticles are embedded in gold matrix; resulting in a combination of the properties from both gold and magnetic nanoparticles. Such nanoparticle can be dragged by magnetic field gradient as well as exhibits surface plasmon resonance from gold.

We fabricated these nanoparticles through template directed synthesis. Anodic aluminum oxide (AAO) has been utilized to generate very large area templates with feature size ranging from 20 nm to 100 nm. Thick and ultra thin AAO templates have been successfully fabricated by anodization. The anodization process of ultra thin AAO has been studied. It has been found that voids are formed on the interface between AAO and the substrate. This unique feature can be attributed to the stress-induced localized delamination of AAO from Si substrate. Multilayered and granular nanodisks have been fabricated by evaporation and

electrodeposition into the AAO templates. Using thick AAO template, multilayered or granular nanodisks are deposited through electrodeposition. A one-bath electrolyte has been developed to deposit both gold and magnetic materials (Co and Fe). Pillar-template has also been generated using the thick AAO template, and is employed to fabricate nanodisks in large quantity. The designed properties have been achieved, including high moment, low remanence and tunable saturation field.

REFERENCES

1. Arruebo, M., et al., *Magnetic nanoparticles for drug delivery.* Nano Today, 2007. **2**(3): p. 22-32.
2. Ito, A., et al., *Medical application of functionalized magnetic nanoparticles.* Journal of Bioscience and Bioengineering, 2005. **100**(1): p. 1-11.
3. Baby, T.T. and S. Ramaprabhu, *SiO2 coated Fe3O4 magnetic nanoparticle dispersed multiwalled carbon nanotubes based amperometric glucose biosensor.* Talanta. **80**(5): p. 2016-2022.
4. Jordan, A., et al., *Presentation of a new magnetic field therapy system for the treatment of human solid tumors with magnetic fluid hyperthermia.* Journal of Magnetism and Magnetic Materials, 2001. **225**(1-2): p. 118-126.
5. Graham, D.L., H.A. Ferreira, and P.P. Freitas, *Magnetoresistive-based biosensors and biochips.* Trends in Biotechnology, 2004. **22**(9): p. 455-462.
6. Pankhurst, Q.A., et al., *Applications of magnetic nanoparticles in biomedicine.* Journal of Physics D-Applied Physics, 2003. **36**(13): p. R167-R181.
7. Tartaj, P., et al., *The preparation of magnetic nanoparticles for applications in biomedicine.* Journal of Physics D-Applied Physics, 2003. **36**(13): p. R182-R197.
8. An-Hui, L., E.L. Salabas, and S. Ferdi, *Magnetic Nanoparticles: Synthesis, Protection, Functionalization, and Application.* Angewandte Chemie International Edition, 2007. **46**(8): p. 1222-1244.
9. Lu, A.H., E.L. Salabas, and F. Schuth, *Magnetic nanoparticles: Synthesis, protection, functionalization, and application.* Angewandte Chemie-International Edition, 2007. **46**(8): p. 1222-1244.
10. Chastellain, M., A. Petri, and H. Hofmann, *Particle size investigations of a multistep synthesis of PVA coated superparamagnetic nanoparticles.* Journal of Colloid and Interface Science, 2004. **278**(2): p. 353-360.
11. Cullity, B.D. and C.D. Graham, *Introduction to magnetic materials*. 2nd ed. 2009: John Wiley & Sons, Inc. p. 183.
12. Barbillon, G., et al., *Electron beam lithography designed chemical nanosensors based on localized surface plasmon resonance.* Surface Science, 2007. **601**(21): p. 5057-5061.
13. Malek, C.K. and V. Saile, *Applications of LIGA technology to precision manufacturing of high-aspect-ratio micro-components and -systems: a review.* Microelectronics Journal, 2004. **35**(2): p. 131-143.
14. Li, J.-H., et al., *Fabrication and characterization of a novel TiO2 nanoparticle self-assembly membrane with improved fouling resistance.* Journal of Membrane Science, 2009. **326**(2): p. 659-666.
15. Gorelick, S., et al., *Fabrication of microfluidic devices using MeV ion beam Programmable Proximity Aperture Lithography (PPAL).* Nuclear Instruments

and Methods in Physics Research Section B: Beam Interactions with Materials and Atoms, 2008. **266**(10): p. 2461-2465.
16. Jung, B., et al., *Scanning probe lithography for fabrication of Ti metal nanodot arrays.* Ultramicroscopy. **110**(6): p. 737-740.
17. Kim, K., M. Kim, and S.M. Cho, *Pulsed electrodeposition of palladium nanowire arrays using AAO template.* Materials Chemistry and Physics, 2006. **96**(2-3): p. 278-282.
18. Lei, Y., W. Cai, and G. Wilde, *Highly ordered nanostructures with tunable size, shape and properties: A new way to surface nano-patterning using ultra-thin alumina masks.* Progress in Materials Science, 2007. **52**(4): p. 465-539.
19. Masuda, H. and M. Satoh, *Fabrication of gold nanodot array using anodic porous alumina as an evaporation mask.* Japanese Journal of Applied Physics Part 2-Letters, 1996. **35**(1B): p. L126-L129.
20. Li, A.P., et al., *Hexagonal pore arrays with a 50-420 nm interpore distance formed by self-organization in anodic alumina.* Journal of Applied Physics, 1998. **84**(11): p. 6023-6026.
21. Jessensky, O., F. Muller, and U. Gosele, *Self-organized formation of hexagonal pore structures in anodic alumina.* Journal of The Electrochemical Society, 1998. **145**(11): p. 3735-3740.
22. Masuda, H., F. Hasegwa, and S. Ono, *Self-ordering of cell arrangement of anodic porous alumina formed in sulfuric acid solution.* Journal of The Electrochemical Society, 1997. **144**(5): p. L127-L130.
23. Keller, F., M.S. Hunter, and D.L. Robinson, *Structural Features of Oxide Coatings on Aluminum.* Journal of The Electrochemical Society, 1953. **100**(9): p. 411-419.
24. Li, F.Y., L. Zhang, and R.M. Metzger, *On the growth of highly ordered pores in anodized aluminum oxide.* Chemistry of Materials, 1998. **10**(9): p. 2470-2480.
25. Polyak, B. and G. Friedman, *Magnetic targeting for site-specific drug delivery: applications and clinical potential.* Expert Opinion on Drug Delivery, 2009. **6**(1): p. 53-70.
26. Plank, C., et al., *The magnetofection method: Using magnetic force to enhance gene delivery.* Biological Chemistry, 2003. **384**(5): p. 737-747.
27. Namdeo, M., et al., *Magnetic Nanoparticles for Drug Delivery Applications.* Journal of Nanoscience and Nanotechnology, 2008. **8**(7): p. 3247-3271.
28. Gazeau, F., M. Levy, and C. Wilhelm, *Optimizing magnetic nanoparticle design for nanothermotherapy.* Nanomedicine, 2008. **3**(6): p. 831-844.
29. Ino, K., M. Okochi, and H. Honda, *Application of Magnetic Force-Based Cell Patterning for Controlling Cell-Cell Interactions in Angiogenesis.* Biotechnology and Bioengineering, 2009. **102**(3): p. 882-890.
30. de Vries, A.H.B., et al., *Micro magnetic tweezers for nanomanipulation inside live cells.* Biophysical Journal, 2005. **88**(3): p. 2137-2144.
31. Chiou, C.H., et al., *New magnetic tweezers for investigation of the mechanical properties of single DNA molecules.* Nanotechnology, 2006. **17**(5): p. 1217-1224.
32. Kanger, J.S., V. Subramaniam, and R. van Driel, *Intracellular manipulation of chromatin using magnetic nanoparticles.* Chromosome Research, 2008. **16**(3): p. 511-522.

33. Nordling, J., et al., *Giant Magnetoresistance Sensors. 1. Internally Calibrated Readout of Scanned Magnetic Arrays.* Analytical Chemistry, 2008. **80**(21): p. 7930-7939.
34. Millen, R.L., et al., *Giant Magenetoresistive Sensors. 2. Detection of Biorecognition Events at Self-Referencing and Magnetically Tagged Arrays.* Analytical Chemistry, 2008. **80**(21): p. 7940-7946.
35. Tamanaha, C.R., et al., *Magnetic labeling, detection, and system integration.* Biosensors & Bioelectronics, 2008. **24**(1): p. 1-13.
36. Brown, W.F., *Thermal Fluctuations of a Single-Domain Particle.* Physical Review, 1963. **130**(5): p. 1677.
37. Bedanta, S. and W. Kleemann, *Supermagnetism.* Journal of Physics D-Applied Physics, 2009. **42**(1): p. 28.
38. Mornet, S., et al., *Magnetic nanoparticle design for medical applications.* Progress in Solid State Chemistry, 2006. **34**(2-4): p. 237-247.
39. Safarik, I. and M. Safarikova, *Use of magnetic techniques for the isolation of cells.* Journal of Chromatography B, 1999. **722**(1-2): p. 33-53.
40. Hu, W., et al., *High-moment antiferromagnetic nanoparticles with tunable magnetic properties.* Advanced Materials, 2008. **20**(8): p. 1479-+.
41. Koh, A.L., et al., *Preparation, structural and magnetic characterization of synthetic anti-ferromagnetic (SAF) nanoparticles.* Philosophical Magazine, 2008. **88**(36): p. 4225-4241.
42. Ross, C.A., et al., *Magnetic behavior of lithographically patterned particle arrays (invited).* Journal of Applied Physics, 2002. **91**(10): p. 6848.
43. Yin, Y., et al., *Formation of Hollow Nanocrystals Through the Nanoscale Kirkendall Effect.* Science, 2004. **304**(5671): p. 711-714.
44. Thouless, M.D., J.W. Hutchinson, and E.G. Liniger, *Plane-strain, buckling-driven delamination of thin films: Model experiments and mode-II fracture.* Acta Metallurgica et Materialia, 1992. **40**(10): p. 2639-2649.
45. Zhang, X.Y., et al., *Advances in contemporary nanosphere lithographic techniques.* Journal of Nanoscience and Nanotechnology, 2006. **6**(7): p. 1920-1934.
46. Hulteen, J.C. and C.R. Martin, *A general template-based method for the preparation of nanomaterials.* Journal of Materials Chemistry, 1997. **7**(7): p. 1075-1087.
47. Guo, L.J., *Nanoimprint lithography: Methods and material requirements.* Advanced Materials, 2007. **19**(4): p. 495-513.

BIOGRAPHICAL STATEMENT

Punnapob Punnakitikashem was born in 1982 in Bangkok, Thailand. He received his B.S. degree in Materials Science from the Chulalongkorn University in 2005, and his Ph.D. in Materials Science and Engineering from the University of Texas at Arlington in 2011. During his study at UTA, he also worked as a research assistant for Dr. Yaowu Hao on several projects and as a teaching assistant for many classes at the MSE department. He also volunteered as an instructor for ASM International Materials Science Camp. His current research interest is in the areas of Thin Film Fabrications and Characterizations, Magnetic Properties, and Synthesis of Nanoparticles.